A Lagrangian Objective Analysis Technique for Assimilating In Situ Observations with Multiple-Radar-Derived Airflow

CONRAD L. ZIEGLER

NOAA/National Severe Storms Laboratory, Norman, Oklahoma

MICHAEL S. BUBAN AND ERIK N. RASMUSSEN

Cooperative Institute for Mesoscale Meteorological Studies, University of Oklahoma, Norman, Oklahoma

(Manuscript received 23 January 2006, in final form 22 September 2006)

ABSTRACT

A new Lagrangian analysis technique is developed to assimilate in situ boundary layer measurements using multi-Doppler-derived wind fields, providing output fields of water vapor mixing ratio, potential temperature, and virtual potential temperature from which the lifting condensation level (LCL) and relative humidity (RH) fields are derived. The Lagrangian analysis employs a continuity principle to bidirectionally distribute observed values of conservative variables with the 3D, evolving boundary layer airflow, followed by temporal and spatial interpolation to an analysis grid. Cloud is inferred at any grid point whose height $z > z_{\mathrm{LCL}}$ or equivalently where RH $\geq 100\%$. Lagrangian analysis of the cumulus field is placed in the context of gridded analyses of visible satellite imagery and photogrammetric cloud-base area analyses. Brief illustrative examples of boundary layer morphology derived with the Lagrangian analysis are presented based on data collected during the International H_2O Project (IHOP): 1) a dryline on 22 May 2002; 2) a cold-frontal–dryline "triple point" intersection on 24 May 2002. The Lagrangian analysis preserves the sharp thermal gradients across the cold front and drylines and reveals the presence of undulations and plumes of water vapor mixing ratio and virtual potential temperature associated with deep penetrative updraft cells and convective roll circulations. Derived cloud fields are consistent with satellite-inferred cloud cover and cloud-base locations.

1. Introduction

During May–June 2002, the International H_2O Project (IHOP) sampled drylines (DLs) and cold fronts (CFs) on the U.S. southern Great Plains with an array of mobile observing systems to document the boundary layer (BL) processes that force the initiation of thunderstorms near these mesoscale boundaries (Weckwerth et al. 2004; Weckwerth and Parsons 2006). In response to the objective of improving warm-season convection forecasts, one focus of IHOP was to map the evolving fields of cloud-scale water vapor, temperature, and airflow in the BL and to learn how these factors control the initiation or suppression of deep, moist convection.

Corresponding author address: Dr. Conrad L. Ziegler, National Severe Storms Laboratory, Forecast Research and Development Division, 120 David L. Boren Blvd., Norman, OK 73072.
E-mail: conrad.ziegler@noaa.gov

DOI: 10.1175/MWR3396.1

Determining the susceptibility of the local boundary layer airflow to cumulus formation and convection initiation (CI) requires 3D, time-dependent fields of lifting condensation level (LCL) and the level of free convection (LFC). The need for spatially variable, evolving parcel stability parameters in turn requires fields of water vapor mixing ratio and potential temperature in the radar analysis domain, from which relative humidity and the parcel stability parameters can be derived. Additionally, output virtual potential temperature fields are useful for analyzing BL dynamics. A difficult aspect of the analysis of state variables in the BL is that in situ data from mobile mesonets, aircraft, and soundings are dense along-track while limited to one spatial dimension. The track-normal sparseness of the mobile observations requires an objective analysis (OA) method that can fill these data voids, while preserving a level of detail in the along-track direction.

To mitigate the effects of in situ data sparseness, an

advection conservation or "Lagrangian" principle is applied using trajectories derived from highly resolved 3D, time-dependent airflow to simulate the displacement of BL observations following the local airflow. Under the assumption that a BL temperature or moisture variable behaves approximately as a local passive tracer of the airflow, an observation may effectively be distributed along an air trajectory that passes through the point of observation. Employing this Lagrangian method to effectively multiply limited observations and reorient measured 1D moisture and temperature gradients along air trajectories, the 3D structure of the BL can thus be approximated given the 4D airflow fields. A Lagrangian analysis technique has been developed to map all available in situ BL data onto the radar analysis grid, and is the subject of this paper. Although the direct benefits of Lagrangian analysis for operational forecasting are limited by the availability of cloud–mesoscale observations, important indirect benefits of Lagrangian analysis include its capability as a new research tool and as a method to determine the type, resolution, and mix of observations required to diagnose the mesoscale conditions conducive to CI and storm evolution. Two cases are chosen to illustrate the Lagrangian analysis: the 22 May 2002 DL and the 24 May 2002 CF–DL "triple point" intersection cases during IHOP.

Few examples of the use of fluid flow and Lagrangian techniques in OA exist, and are typically restricted to the meso–β (20–200 km) and larger scales. For example, conventional atmospheric OA based on distance-dependent weighting may take streamlines into account by adjusting the shape of the spatial weighting function to follow the local airflow direction and curvature (Benjamin and Seaman 1985). However, the latter technique is difficult to adapt for the rather high degree of local variability of curvature following the motion that often characterizes the BL. An extended Kalman filter technique has been developed to assimilate Lagrangian tracer data from floating platforms into oceanographic models (Kuznetsov et al. 2003). The latter Kalman filter method would not be directly applicable to IHOP data, which are obtained from mobile platforms that move relative to the local flow and thus are arranged at angles to trajectories. Instead, the proposed Lagrangian approach distributes in situ BL data along trajectories defined by the local meso–γ (2–20 km) and finer-scale airflow, with along-trajectory time weighting substituting for the along-flow extension of the Benjamin and Seaman (1985) spatial weighting function. The present Lagrangian OA technique combines this along-flow time weighting with conventional observational temporal and spatial weighting (Barnes 1973).

2. Lagrangian objective analysis of thermal variables

The principle of the Lagrangian analysis is to provide 3D spatial mesoscale BL structure by distributing water vapor mixing ratio (q_v), potential temperature (θ), and virtual potential temperature (θ_v) observations along bidirectional 4D trajectories derived from the time-spaced input multi-Doppler analyses. Data values are assigned to discrete locations corresponding to time increments along the trajectories (the latter termed "Lagrangian points"), followed by OA of these "Lagrangian data" to a regular Cartesian grid. A two-pass Barnes interpolation scheme incorporates spatial and temporal weighting to derive the 3D fields of these scalar variables for subsequent diagnostic calculations of LCL and other parcel indices.

The LCL often increases with height due to some degree of mixing of moist BL air parcels with warmer, drier air from an elevated stable layer (Betts 1984). The assumption of a constant LCL by classical parcel theory is unwarranted unless—in rather rare circumstances—the BL is homogeneously well mixed. Vertical circulations associated with juxtaposed, evolving BL updrafts and downdrafts in the presence of vertical shear may bring air parcels from differing origin levels into fairly close proximity (e.g., Fig. 10 of Ziegler and Hane 1993), providing conditions for mixing of the differing source air parcels. On the other hand, organized mesoscale circulations may lift neighboring air parcels from similar origin locations along nearly parallel trajectories (e.g., DL updraft bands in Ziegler et al. 1997), resulting in minimal parcel dilution even if local mixing occurs. Although the Lagrangian analysis presently does not include the effects of subgrid-scale turbulent mixing along individual parcel trajectories, it implicitly treats the smoothing effect of resolvable-scale mixing due to the objective analysis (i.e., weighted averaging) of neighboring air parcels if these have differing origins and contrasting source airmass characteristics.

An array of mobile airborne and ground-based observing platforms has provided airflow and in situ data for input to the Lagrangian analysis. The National Severe Storms Laboratory (NSSL) deployed the SR1 Shared Mobile Atmospheric Research and Teaching (SMART) 5-cm Doppler radar (Biggerstaff et al. 2005) during IHOP. Data from SR1 were combined in post-analysis with closely coordinated observations by the 3-cm "Doppler-on-Wheels" DOW2, DOW3, and XPOL radars (Wurman 2001; Wurman et al. 1997) to synthesize the time-dependent, 3D airflow in the BL. In

situ data were provided by other NSSL-deployed platforms, including up to nine mobile mesonets (Straka et al. 1996; for description of major pre-IHOP upgrades see also Figs. 1 and 4 and related discussion in Ziegler et al. 2004) and a Cross-Chain Loran Atmospheric Sounding System (CLASS; Rust et al. 1990). The NSSL also deployed two digital ground-based cameras for cloud field photogrammetry, one camera with SR1 and the second camera with a sedan at a different location. Additional in situ data were provided by two National Center for Atmospheric Research (NCAR) mobile GPS/Loran Atmospheric Sounding System (GLASS) vehicles and airborne dropsondes, the University of Wyoming King Air (KA; Geerts et al. 2006) and the Naval Research Laboratory (NRL) P-3 (Wakimoto et al. 2006) research aircraft, and a fixed sounding system at the Homestead site in the eastern Oklahoma panhandle.

a. Ground-based mobile radar analysis

The ground-based mobile radar data were extensively edited using SOLO (Oye et al. 1995). Radar editing effected removal of ground targets, weak or range-folded echoes, and widely spaced (i.e., "speckled") echoes, as well as the correction of sweeps for truck orientation relative to true north and the dealiasing of radial velocities. Two internally consistent methods were used to correct radar sweeps for truck orientation. A truck orientation or "rotation angle" correction based on a sun scan algorithm was obtained for the DOW2 radar (Arnott et al. 2003), yielding an accuracy of about 0.1° in azimuth. A second correction for truck orientation was applied to all radars by azimuthally rotating base (0.5° elevation) scan sweeps and matching positions of ground target echoes with mapped positions of tall towers, roadside range fences and power poles, and terrain features such as ridges and drainages (e.g., Fig. 1). The matched ground target echo method for estimating rotation angle correction was previously applied by Wurman and Gill (2000) by comparing DOW base scans with road locations, the main refinement of the present approach being to overlay radar sweeps on road and tall tower locations in a geographical information system (GIS) display and applying orientation angle corrections directly to the input radar sweep files to maximize subjective agreement (Ziegler et al. 2004). The latter rotation angle correction had different estimated accuracies for point and line ground targets, ranging from as large as about 1/4 beamwidth (i.e., 0.25° for DOWs and 0.4° for SR1) for single point targets (e.g., a tall tower) to as small as about 0.1° for grouped point targets or line targets due to effectively least squares fitting multiple point estimates. Favorable direct comparisons of both methods (N. Arnott 2004, personal communication) supported application of the ground target and the sun scan correction methods.

Edited radar radial velocity and reflectivity data are spatially interpolated to the analysis grid with REORDER (Oye et al. 1995) employing Barnes weighting (Barnes 1973; Koch et al. 1983). Data positions are adjusted in time-to-space to approximate the ground-relative motions of pre-CF updrafts, reflectivity cores, and misovortices using reference frames of 190° at 15 m s^{-1} (22 May) and 225° at 4.5 m s^{-1} (24 May) respectively. The isotropic Barnes weighting function takes the form $w = \exp(-r^2/\kappa)$, where r is the distance from a grid point to a datum and κ is the spatial smoothing parameter. For chosen input values of amplitude response $D_0 = 0.05\%$ at the "target wavelength" $L = 0.4$ km with $\lambda^* = 1.0$, the smoothing parameter $\kappa = 0.0486$ (Koch et al. 1983). The resulting theoretical radar analysis response of the Barnes filter is ~80% at 1.4 km (Table 1; Fig. 2). In the final analysis step, the CEDRIC radar synthesis program is applied using either dual-Doppler or overdetermined three- or four-radar dual-Doppler (i.e., "two equation") schemes to derive the 3D vector airflow from multiple-Doppler radial velocities (Mohr et al. 1986). Neglecting very small terrain-induced vertical motions of surface winds, the anelastic mass continuity equation is vertically integrated from $w = 0$ at ground level.

Since the radar gate spacings in azimuth and elevation at range tend to substantially exceed the radial gate spacing (67 m for SR1, 75 m for DOW2 and DOW3, 210 m for XPOL), the former dominate the latter and greatly decrease the effective spatial radar resolution. To clarify terminology, the reader should note that grid "resolution" here refers only to the ability of the grid to depict a given sinusoid whereas the previously referenced analysis "response" specifically refers to the amplitude ratio of the output (grid interpolated) to input (observed) sinusoid. The grid spacing has been chosen to be consistent with nominal gate spacings at 30-km range of 1° in azimuth and 0.5° in elevation, thereby increasing data density for spatial interpolation at shorter ranges while maintaining a spatially uniform analysis response in wavelength. The corresponding horizontal and vertical radar analysis grid spacings are 0.5 and 0.25 km, respectively, allowing resolution of horizontal wavelengths greater than 1 km and BLs deeper than 0.5 km. Since the Lagrangian analysis to be described below shares the radar analysis grid, the chosen grid is also sufficient to depict ramp-function changes of water vapor mixing ratio over ~0.5–1 km horizontal distances that are commonly observed by mobile mesonets and aircraft. The spatial dimensions of the Cartesian radar analysis domain are 50 km × 50 km

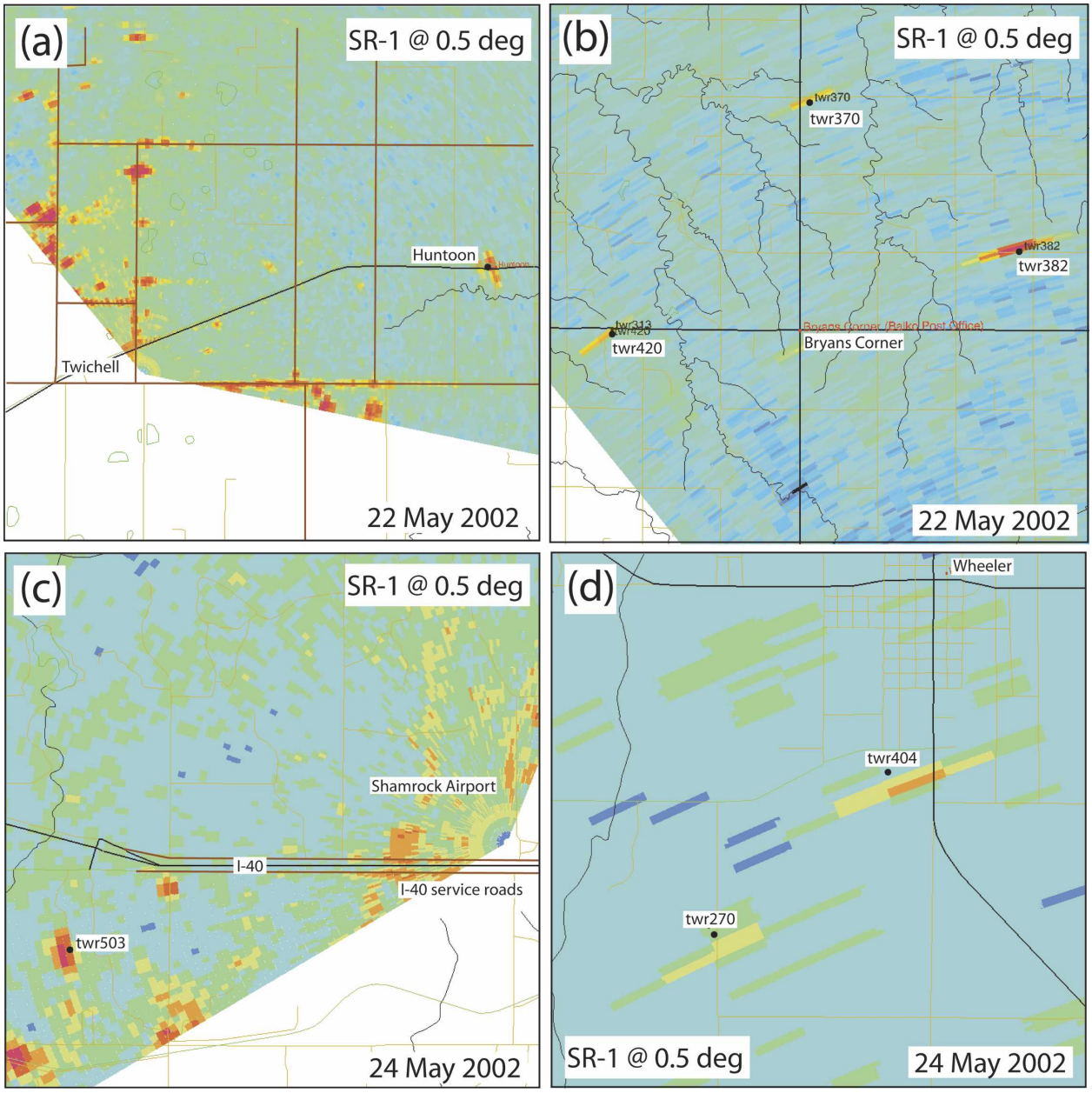

FIG. 1. Ground target echo patterns in rotated but otherwise unedited SR-1 reflectivity (dBZ) at 0.5° elevation in the 22 May and 24 May 2002 IHOP cases discussed in the text. (a) Near-surface echoes in the vicinity of the radar site on 22 May; (b) tall tower echoes on 22 May; (c) near-surface echoes in the vicinity of the radar site on 24 May; and (d) tall tower echoes on 24 May. The panels were generated with an Interactive Data Language (IDL)-based 3D GIS program written by one of the coauthors (E. Rasmussen) that projects roads, tall towers, rivers and creeks, geographic place names, and other overlay information on an image background (Ziegler et al. 2004). Tall towers are denoted by "twrhhh," where "hhh" is tower height (ft).

horizontally and 2.5 km vertically in the 22 May and 24 May cases.

As an alternative to the filtering parameter and grid spacing chosen for the present radar analysis, the recommendations of Pauley and Wu (1990) and Trapp and Doswell (2000) could be followed to choose a more conservative (i.e., larger) value of the Barnes filtering parameter and a smaller grid spacing (e.g., Arnott et al. 2006). After determining the effective average data spacing $\delta D \sim 0.2$ km that corresponds to the previously assumed $\kappa = 0.0486 = 1.77\delta D^2$ (Pauley and Wu 1990), a four-radar analysis test has been conducted in the 24 May case assuming a more conservative value of average data spacing $\delta D = 0.5$ km (e.g., Trapp and Doswell

TABLE 1. Barnes filter parameters and response values (e.g., 100% is ideal response) at selected wavelength (km) or period (min) for the temporal and spatial Barnes weighting in the radar and Lagrangian objective analyses in the 22 May and 24 May 2002 IHOP case studies. Entries correspond to the second-pass values for the Langrangian analysis and the one-pass radar analysis, respectively. The filter parameter (Barnes 1973; Koch et al. 1983) is denoted by κ for spatial weighting and τ for temporal weighting. The radar analysis applies one filtering pass of the Barnes interpolation (same filtering parameter for both cases), while the convergence parameter γ equals 0.3 for the two-pass Lagrangian objective analysis. The corresponding response functions are displayed in Fig. 1. Distances in parentheses in the "temporal Lagrangian point" rows are wavelengths L_U (km) equivalent to the indicated periods T (min) via time-to-space conversion (i.e., $T = L/U$) as described in the text. The velocity scales corresponding to the tabulated L values in the "temporal Lagrangian point" rows are $U = 15$ and 7 m s^{-1} in the 22 and 24 May cases, respectively.

Type of interpolation	Barnes filtering parameter	Wavelength (km) or period (min) for 5% response	Wavelength (km) or period (min) for 80% response
Spatial Lagrangian point	$\kappa_s = 0.076$ (22 May)	0.25 km	0.75 km
(second-pass response)	$\kappa_s = 0.124$ (24 May)	0.35 km	1 km
Temporal initial condition	$\tau_i = 364363$ (22 May)	10 min	29 min
(second-pass response)	$\tau_i = 714113$ (24 May)	14 min	41 min
Temporal Lagrangian point	$\tau_L = 640856$ (22 May)	13 min (~12 km)	39 min
(second-pass response)	$\tau_L = 1457374$ (24 May)	20 min (~8 km)	58 min
Spatial radar observation	$\kappa = 0.0486$ (22 and 24 May)	0.4 km	1.4 km
(one-pass response)			

2000) for which $\kappa = 0.442$. The resulting radar analysis using the latter conservative filtering parameter value produces a smoother analysis as expected, and in particular reduces the resolution of the shallow convective BL and weakens vertical velocities. On the other hand, the overall horizontal BL structure in both analyses is broadly very similar, in turn suggesting that the response difference between the control and test analyses is concentrated at wavelengths shorter than the predominant BL roll circulations. The present grid spacing choice appears to be sufficiently small to resolve the BL updrafts that are demonstrated by subsequent research to force the development of observed cumulus clouds (e.g., Ziegler et al. 2007).

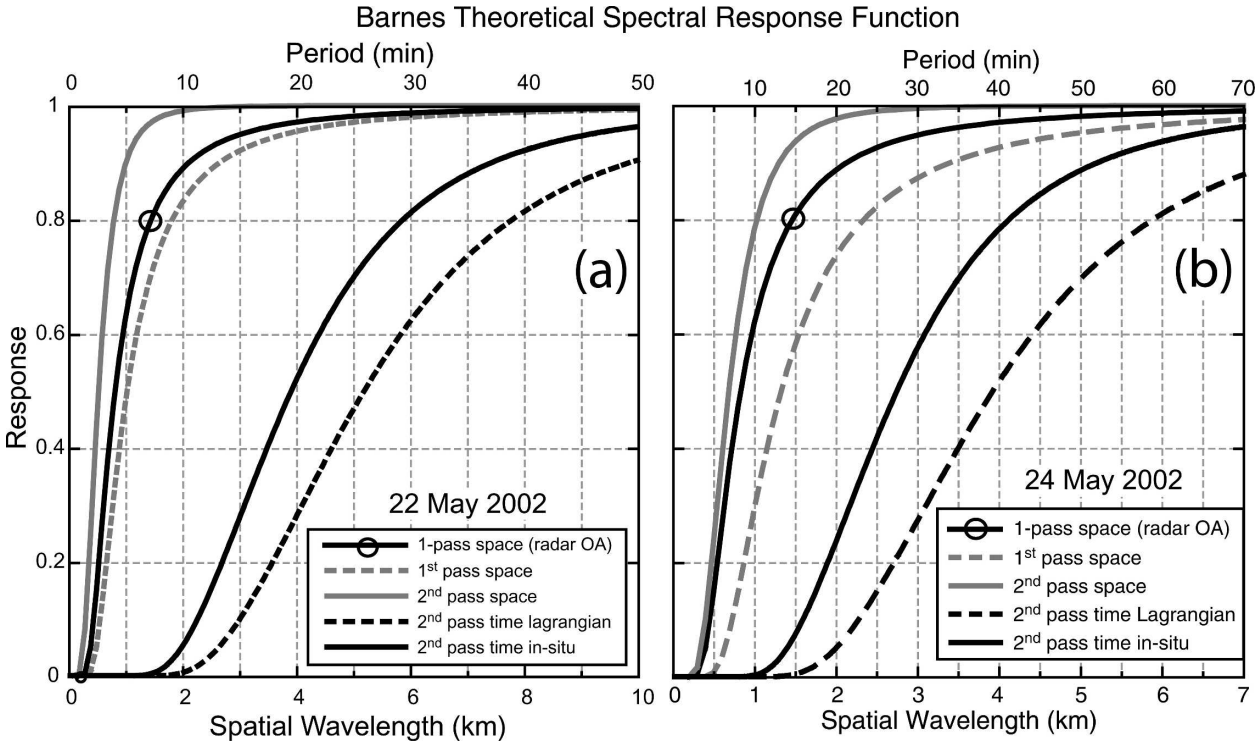

FIG. 2. Amplitude response vs input wavelength (km) of the Barnes objective analysis weighting function: (a) 22 May 2002 analysis; (b) 24 May 2002 analysis. Barnes filtering parameters and responses at selected periods or wavelengths are listed in Table 1. Circled curve denotes one-pass radar OA response.

The shallowness of the post-CF air mass relative to the SR1 beam at range in the 24 May case results in rather poor resolution and downward extrapolation errors in the lowest sweep through the post-CF layer. Additionally, certain dual-Doppler pairs including SR1 produce erroneous velocity estimates due to small between-beam angles at some analysis grid points. The CEDRIC program tests the location of each grid column relative to a best-fit line that proxies the actual CF position. To mitigate the post-CF sampling errors, four-radar analyses including SR1 observations are employed southeast (ahead) of the CF while three-radar analyses that exclude SR1 are applied northwest of (behind) the CF.

b. Trajectory calculation and Barnes analysis

A key aspect of the Lagrangian analysis is the integration of a pair of upstream and downstream air trajectories from each datum location (Fig. 3). Air trajectories are calculated from the 3D, time-dependent, ground-relative airflow analyses with a quadratic Runge–Kutta predictor–corrector scheme (McCalla 1967, 310–312) with a time step of 6 s, converging in three iterations. Gridded wind components are linearly interpolated in time to the current trajectory time from adjacent wind analysis time levels, followed by trilinear spatial interpolation to the current Lagrangian point. To fill data voids, the length of a trajectory should be large enough to span the distances between the mobile mesonet and aircraft legs while also allowing sufficient numbers of trajectories to reach the lateral boundaries of the analysis domain at all analysis levels (e.g., Fig. 3a). Horizontal wind speed exerts a primary control on trajectory length, thus requiring longer trajectory duration in weaker winds. Trajectories that originate at interior grid points and are based on reference soundings (described in detail in section 2c) are only initialized in a convective BL, not in an elevated residual layer (ERL), thus requiring a longer trajectory duration to extend from the initial grid point through a horizontally extensive ERL. The values of either an observation or a grid-column sounding at an initial trajectory point are assigned to that trajectory at all of its Lagrangian points, effectively assuming conservation following the local air parcel motion.

The Lagrangian OA employs spatial and temporal multipass Barnes (1973) weighting to interpolate the Lagrangian data to the analysis grid[1] (e.g., Fig. 3b). Mobile mesonet data are interpolated in 2D to obtain the surface-level analysis, while varying combinations of Lagrangian grid-column sounding, mobile sounding and dropsondes, and aircraft data are employed in the 3D objective analysis above the surface (Fig. 3b). The exponential weighting function is used to average in space and time following its conventional application (Barnes 1973), but also to effectively relax the local conservation assumption by reducing the weight with increasing time along the trajectory. The first-pass Barnes weighting function (Barnes 1973) takes the form

$$w_1 \equiv w_s \times w_i \times w_L = \exp\left[-\left(\frac{r^2}{\kappa_s}\right) - \left(\frac{t_i^2}{\tau_i}\right) - \left(\frac{t_L^2}{\tau_L}\right)\right], \quad (1)$$

where r is the radial distance separating a Lagrangian point and a grid point, κ_s is the spatial smoothing parameter, t_L and t_i are, respectively, the accumulated trajectory integration time and the time difference between an in situ observation and the nominal map time, and τ_L and τ_i are the temporal smoothing parameters. The spatial weighting term (i.e., w_s) imposes filtering in the wavelength domain and is isotropic (i.e., independent of orientation of the radial displacement vector) to avoid distorting curved features (Trapp and Doswell 2000) such as CF or DL surfaces, the BL transition zone, and updraft plumes. The temporal in situ weighting term (i.e., w_i) filters in the frequency domain (Barnes 1973), damping local time fluctuations. Conversely, the temporal along-trajectory weighting term (i.e., w_L) imposes filtering of poorly resolved spatial along-flow scales in a time-to-space sense and is analogous to the concept of Lagrangian decorrelation in the turbulent BL (e.g., Dosio et al. 2005). Temporal along-trajectory weighting of closely neighboring upstream and downstream trajectories approximates along-flow gradients, thus effectively relaxing the previously mentioned assumption of conservation following the local air parcel motion.

To restore additional analysis detail, a second or "correcting" Barnes analysis pass (Koch et al. 1983) is applied to the entire 3D domain. The first pass analysis values are trilinearly interpolated to trajectory points, and the difference between the interpolated and Lagrangian data values are calculated. The first-pass differences are then interpolated to the grid using the modified Barnes function

$$w_2 = \exp\left[-\left(\frac{r^2}{\gamma\kappa_s}\right) - \left(\frac{t_i^2}{\gamma\tau_i}\right) - \left(\frac{t_L^2}{\gamma\tau_L}\right)\right], \quad (2)$$

where the convergence parameter $\gamma = 0.3$ premultiplies the smoothing parameters in Eq. (1). Following objective analysis with weighting prescribed by Eq. (2), the difference field is added to the first-pass field to obtain

[1] In contrast, the radar OA employed one-pass Barnes weighting with a different spatial weighting coefficient.

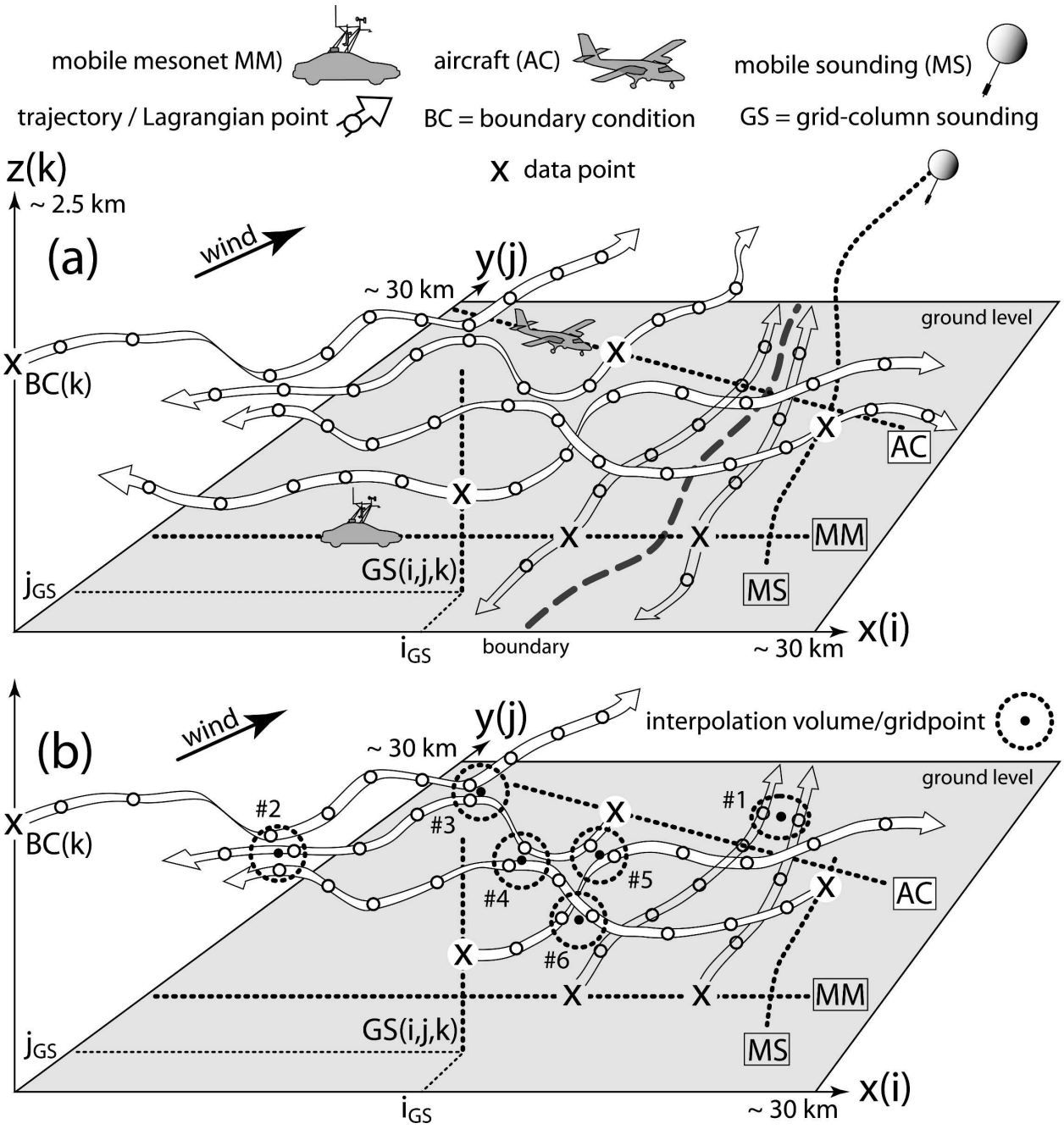

FIG. 3. Illustration of the Lagrangian analysis technique (see also Fig. A1). (a) Data distribution along trajectories defined by the 3D airflow; (b) Lagrangian objective analysis. Data sources are mobile mesonets (MM), aircraft (AC), mobile soundings (MS), grid-column soundings (GS), and boundary condition (BC). Forward (downstream) and backward (upstream) trajectories are denoted as bidirectional arrowhead-tipped ribbons proceeding from data locations denoted by "X" symbols. Small black circles denote Lagrangian data locations. Surface objective analysis involves MM-only weighting, while BL objective analysis may include weighting of one or more of the GS, AC, MS, and BC data. Several of the possible data pairings during gridpoint interpolation are illustrated in (b), including MM/MM (#1) for surface analysis and AC/MS/BC (#2), AC/BC (#3), AC/MS (#4), GS/AC (#5), and GS/MS (#6) for BL analysis. The gridpoint interpolation scheme requires a minimum of three unique trajectories within the spatial interpolation volume (denoted by dashed circle) centered on an analysis grid point (denoted by black dot).

the second-pass field. The first Barnes analysis pass is referred to as a "smoothing" pass, since it provides a relatively smooth first-guess field that is subsequently refined by the correcting pass. The Barnes analysis converges rapidly and requires only two passes in the present application.

c. *Grid-column and lateral boundary soundings from airmass-dependent reference soundings*

The advected and objectively analyzed in situ surface mobile mesonet observations provide by far the greatest information on horizontal structure of the surface layer. In contrast, aircraft traverses and soundings yield vital though relatively low density information on the structure of the BL. Thus, as described in greater detail below, the Lagrangian analysis extrapolates the dense surface information vertically in grid columns using "reference soundings" to describe the bulk profiles of temperature and vapor mixing ratio in the BLs on either side of the DL and behind the CF. The "pseudodata" in these "grid-column soundings" are then distributed and objectively analyzed to supplement in situ data for the purpose of enhancing the 3D analysis of the BL. All grid-column soundings are assigned the chosen nominal map time, resulting in the initial condition time-difference weight [i.e., the third exponential term in Eqs. (1) and (2) above] having a value of unity.

Weckwerth et al. (1996) showed that measured horizontal profiles of θ and q_v in the lower BL are positively correlated with vertical velocity, implying that horizontal convective roll updrafts lift warm, moist air from near ground into the BL. Ziegler et al. (1997) effectively confirmed the finding of Weckwerth et al. (1996), employing cloud-scale DL simulations to demonstrate that θ_v and q_v in mesoscale BL updrafts are correlated to near-surface conditions owing to vertical advection that creates warm, moist updraft plumes. To test the notion of correlated surface and BL thermal variables in the 22 May and 24 May cases, KA research aircraft data obtained in BL updrafts were compared to the range of mobile soundings and surface mobile mesonet observations in the same area and time period as the aircraft transects (Fig. 4). Since aircraft transects are neither located directly above mobile mesonet legs nor coincident with sounding locations, it is possible to compare only the ranges of surface conditions and sounding profiles against aircraft measurements rather than directly validating correlations of surface and updraft properties. Because of the probable dominance of sensible over latent surface layer heat fluxes (i.e., convective BL with surface vegetation under stress), the BLs are strongly superadiabatic in the lowest 200–300 m and well mixed in vapor mixing ratio (Fig. 4). The correlation of surface and BL potential temperature and vapor mixing ratio values justifies the adoption of "reference soundings" to represent the mixed-layer character of the BL (e.g., heavy curves in Fig. 4).

A reference sounding composed of potential temperature and vapor mixing ratio profiles from the surface to the top of the analysis domain (2.5 km) is derived by compositing a mobile sounding with aircraft and mobile mesonet traverses to optimally represent each BL airmass under a range of measured surface conditions (Fig. 4). Exploiting the findings of Weckwerth et al. (1996) and Ziegler et al. (1997) and the correlation between thermal properties of the surface and BL from IHOP data (e.g., Fig. 4), the Lagrangian analysis adjusts the airmass-dependent reference soundings in the convective BL to obtain grid-column soundings in mesoscale updraft regions in the interior of the analysis domain as detailed below in the following paragraph. On 22 May the pre- and post-DL convective BL depths (i.e., the grid-column depth in the analysis interior) are 0.75 and 2 km, respectively, while on 24 May the post-CF and the pre- and post-DL convective BL depths are 0.75, 1.75, and 1.25 km, respectively. The Lagrangian analysis prescribes lateral boundary conditions (BCs) by imposing the appropriate airmass reference sounding through the entire depth of the analysis grid column via forward trajectories originating from any inflow boundary point (Fig. 3). The data in all grid-column soundings are subsequently advected into adjacent downdrafts following trajectories initiated from the updraft grid points. In this manner, data from BL updrafts may be objectively combined with other descending parcels from an overlying stable layer to permit entrainment drying effects in downdrafts.

Grid-column soundings in convective BL updrafts are obtained by two different approaches in the Lagrangian analysis, depending on the type of BL. The two grid-column sounding types are differentiated according to location, either 1) pre-CF (i.e., BLs east and west of the DL as illustrated in Figs. 4a–d) or 2) post-CF (e.g., Figs. 4e,f). In the pre-CF case, the local grid-column soundings are obtained by averaging (i.e., mixing) percentages of the moist- and dry-side reference soundings on mixing lines (e.g., Betts 1984; Ziegler and Hane 1993) with an offset based on the local surface analysis mixing ratio value. For example in the 24 May case, if the moist (dry) side surface reference sounding value is 10 (8) g kg^{-1} (Fig. 4c) and the local, grid-column 2D surface analysis value is 9.5 g kg^{-1} (e.g., within the moist-side mobile mesonet observational range; Fig. 4c), the resulting grid-column sounding

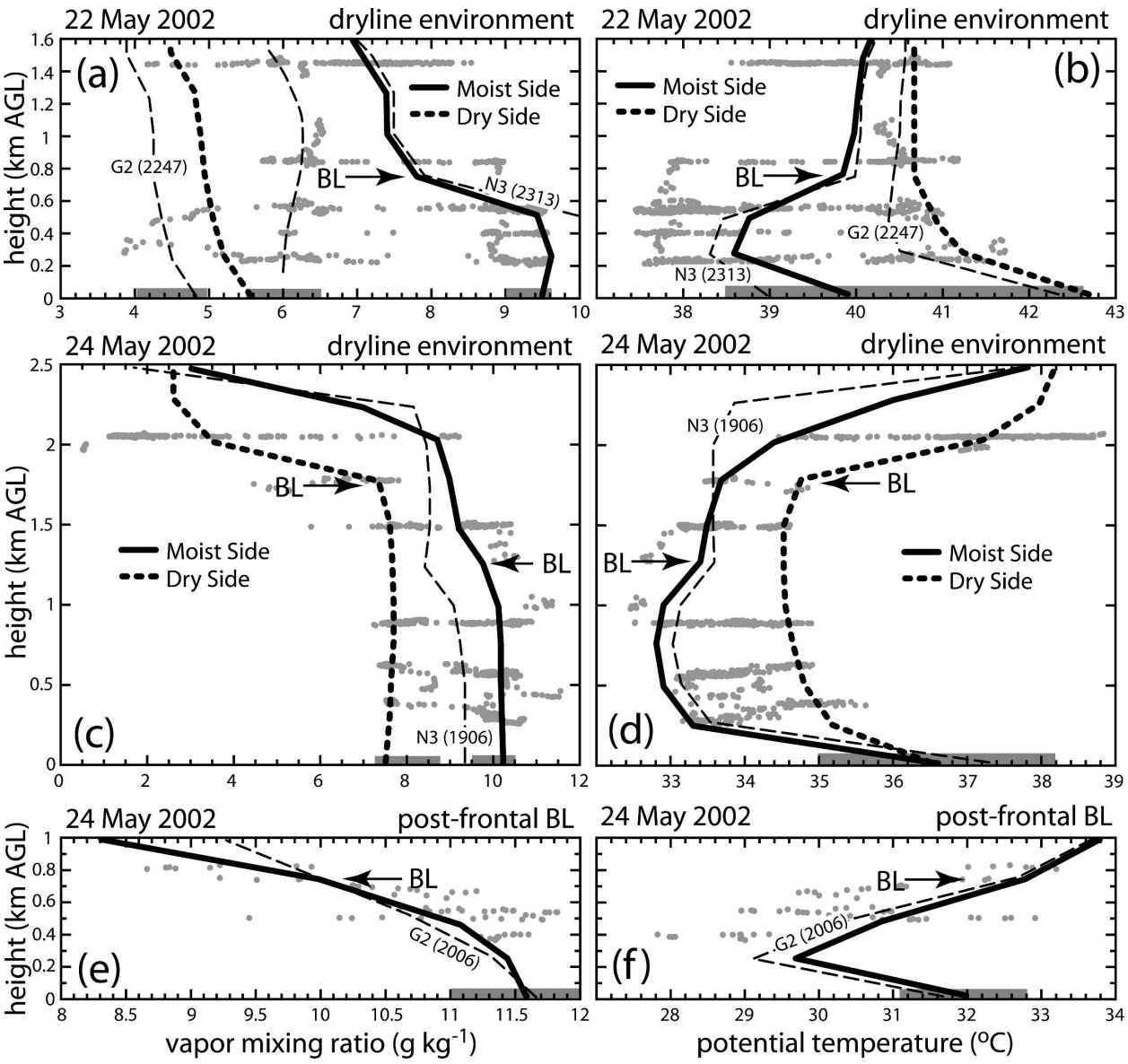

FIG. 4. Reference soundings employed in the Lagrangian analyses for the 22 May and 24 May 2002 IHOP cases: (a) 22 May vapor mixing ratio (q_v) in the dryline environment; (b) 22 May potential temperature (θ); (c) q_v in the dryline environment (24 May); (d) θ (24 May); (e) q_v in the postfrontal BL (24 May); (f) postfrontal θ (24 May). Although all reference soundings extend to 2.5 km, only the portion in the height range of aircraft data is shown. The heavy solid and dashed lines are the reference soundings on the dry and moist sides of the dryline respectively [(a)–(d)], while the solid curves in (e), (f) are the reference soundings in the postfrontal BL. Gray dots locate KA observations in updrafts >0.1 m s^{-1} during the periods 2230 UTC 22 May to 0000 UTC 23 May [(a), (b)] and 1904–1951 UTC 24 May [prefrontal BL in (c), (d); postfrontal BL in (e), (f)]. The thick gray bands at the bottom of each panel denote ranges of values measured by all MMs in a given air mass during the period of the KA traverses, while thin dashed curves are selected mobile soundings. These mobile mesonet, sounding, and aircraft data are used to subjectively define the reference soundings. The dry sector mobile sounding on 24 May was determined from KA and MM data only. The postfrontal reference sounding matches the dry-side sounding above 1 km on 24 May (not shown).

would consist of a mixture of 75% of the moist side reference sounding and 25% of the dry side reference sounding mixing ratios. Consistent with the latter example, the q_v and θ values in the BL of the 1906 M-CLASS sounding are between the dry and moist side reference sounding values though closer to the latter (Figs. 4c,d). In the post-CF case, it is assumed that vertical top-down entrainment mixing of warm, dry air from above the post-CF inversion into the post-CF convective BL is strongly suppressed by static stability.

Thus in contrast to the pre-CF case, which parameterizes mixing across the DL and moist BL inversion, a grid-column sounding in the post-CF case is instead derived from the sum of the reference sounding value and the difference between the local 2D surface analysis and reference sounding values weighted linearly from zero at the reference sounding depth to unity at the surface. A grid-column sounding value is specified at grid level k provided $w > 0$ at all levels from 0.25 km (level 2) through level k, the top level not exceeding the convective BL depth of the given air mass.

d. Lagrangian analysis summary

An overview description of the Lagrangian analysis is presented here, with radar wind analysis, trajectories, and reference and grid-column soundings described earlier in section 2, while a more detailed overview is presented in the appendix. In summary, the Lagrangian analysis is implemented in five steps: 1) derive airmass-specific reference soundings (described in section 2c as illustrated in Fig. 4), hole-fill radar winds, and filter and subsample (i.e., decimate) in situ time series observations; 2) generate trajectories from in situ data locations (section 2b) and initialize trajectories with data values (Fig. 3a); 3) distribute mobile mesonet (MM) observations on surface trajectories and perform a surface Barnes OA (Figs. 3a,b); 4) impose reference soundings through the interior convective BL by adjusting a local reference sounding according to the local surface analysis value and also impose full-depth unadjusted reference soundings on lateral inflow boundaries (described in section 2c), then distribute interior and lateral boundary grid-column sounding data along trajectories (Fig. 3a); and 5) perform a 3D, two-pass Barnes OA of the combined in situ and grid-column sounding trajectory data (Fig. 3b). To increase the total number of (sparse) in situ data, a particular Lagrangian analysis includes all available observations within an input time window centered on a chosen nominal analysis time.

A rising air parcel achieves water saturation provided its local LCL value is smaller than the altitude of the parcel's trajectory (Ziegler and Rasmussen 1998), where the condition $Z^* = z/Z_{\mathrm{LCL}} = 1$ is met. Continued upward displacement of the saturated parcel above the LCL would generate supersaturation, represented by the condition $Z^* > 1$. A limitation of the present version of the Lagrangian analysis is that changes of q_v and θ_v due to cloud condensation and evaporation are neglected. An expanded Lagrangian analysis to incorporate parameterized diabatic and subgrid-scale turbulent mixing processes following the motion is under development, though beyond the scope of the present study.

3. In situ, satellite, and ground-based camera observations and analysis

As previously described, Lagrangian analysis produces output fields of water vapor mixing ratio, potential temperature, and water-saturated (i.e., cloud) volumes in the BL. Since the Lagrangian analysis applies all available in situ observations and since all observations (especially mobile mesonet) are needed to effect an analysis, validation of the analysis in the present IHOP cases is difficult. Although the Lidar pour l'Étude des Interactions Aérosols Nuages Dynamique Rayonnement et du Cycle de l'Eau (LEANDRE-II) differential absorption lidar (DIAL) on the P-3 aircraft provided remote measurements of water vapor mixing ratio during IHOP, unfortunately airborne DIAL data from LEANDRE-II are unavailable in the 24 May case. Although fixed vertical profile Raman lidar measurements of water vapor mixing ratio are available from the Homestead site within the intensive observing region (IOR) of the 22 May case, a systematic difference of profiled vapor mixing ratio in comparison with aircraft and surface observations and restriction of the lidar data to heights exceeding 0.5 km AGL (Demoz et al. 2006) renders a validation of the Lagrangian analysis fields at that location unfeasible. Though independent temperature and water vapor mixing ratio measurements are unavailable in the IOR on 24 May, the KA stepped traverse pattern has been analyzed following a simpler OA technique (as described in section 3a) to obtain a simplified BL analysis for comparison with the more complex Lagrangian analysis. Finally, cloud fields from the Lagrangian analysis are validated with gridded *Geostationary Operational Environmental Satellite-8* (*GOES-8*) visible images and cloud-base area analyses determined from a photogrammetric method as described in sections 3b and 3c, respectively.

Toward the goal of validating the Lagrangian analysis, a model could in principle be used to simulate the BL evolution and provide proxy airflow and in situ data for the Lagrangian objective analysis via an observing system simulation experiment (OSSE). Four aspects of the Lagrangian analysis should be considered using model BL simulations: 1) effect of particular in situ sampling patterns conducted by the various mobile platforms; 2) prefiltering of unresolved scales contained in the in situ data and subsampling to make along-trajectory and along-leg data spacing more regular; 3) along-Lagrangian weighting; and 4) space–time weighted objective analysis of the Lagrangian data. Addressing the first aspect would be complicated by the need for a very large ensemble of possible mobile platform legs to rigorously test the performance of the

Lagrangian analysis algorithm (e.g., as a function of road density as well as transect speed and length). To address the second aspect, observed data rates and spatial resolutions as fine as 1 Hz and ~20 m and realistic variances could only be replicated in the proxy in situ data with a very high resolution large eddy simulation (LES) model (e.g., Fedorovich et al. 2004; Dosio et al. 2005). However, conducting an OSSE in the present IHOP cases that contain fronts and drylines (and thus are strongly inhomogeneous BLs) would effectively require the abandonment of conventional periodic lateral BCs in favor of time-dependent larger-mesoscale lateral BCs obtained from either observations or a model. The third and fourth aspects could be meaningfully evaluated with a conventional LES model in cases in which the actual large-scale BL is approximately horizontally homogeneous. Finally, the LES output airflow would need to be prefiltered prior to input into the Lagrangian analysis to impose comparable resolution with the present radar analysis. Given the present capability to evaluate the overall performance of the Lagrangian analysis (e.g., cloud field comparison) and considering the aforementioned complexities of applying LES models to observed conditions, an OSSE study to evaluate the Lagrangian analysis is beyond the scope of the present study.

a. Research aircraft stepped traverse analysis

The 24 May case provides an opportunity to compare KA observations on a dense vertically stepped traverse to the Lagrangian analysis. By comparing a simple, conventional non-Lagrangian OA that includes only KA observations with the more complex Lagrangian analysis including all in situ observations and grid-column soundings in addition to KA data, the overall performance of the Lagrangian OA can be assessed via similarities or differences between the analyses.

The KA observations are objectively analyzed in a vertical cross section following methods described by Ziegler and Rasmussen (1998), with minor adjustments for DL motion and variable leg spacing. A forward-looking video camera recording documents individual cloud penetrations and the visual appearance of the cloud field relative to the KA legs (B. Geerts 2004, personal communication). The analysis origin is chosen to be the penetration location of the CF on the lowest leg, and higher legs are shifted eastward in time-to-space according to the DL motion of 2.8 m s^{-1} and their time lag from the lowest leg. Since the upper two legs contain the ERL top and thus have little correlation to surface DL movement, the two upper legs are shifted in time-to-space by the same amount. To better estimate the top of the convective BL given the lack of a mobile sounding between the surface DL and CF locations, a "pseudoleg" is added at 1.7 km to represent the ERL from the 1906 NSSL M-CLASS sounding at that level. The values of temperature, moisture, and wind on the pseudoleg are perturbed by randomly sampling a normal distribution assumed to represent the natural variability of each parameter along the leg. Objective analysis parameters are adjusted vertically to provide more smoothing at higher levels where legs have larger vertical spacings than the lowest legs. For all $x \leq 5$ km, the horizontal divergence is computed from the x gradient of the front-normal component of the objectively analyzed horizontal flow in the cross section. For all $x > 5$ km, the horizontal divergence is obtained from the (DL-normal) total horizontal component in the cross section.

b. Visible satellite imagery

Visible cloud images from the *GOES-8* satellite were processed and mapped to the radar analysis grid using McIDAS (Lazzara et al. 1999). The origin of each image was adjusted to minimize the position difference between a bright sand bar feature marking a bend in the Red River in the eastern Texas panhandle and the known river location in the McIDAS display (i.e., "dejittering"). Images were then renavigated to the radar analysis grid. The *GOES-8* pixel resolution in the chosen subsector is 1.5 km in latitude and 1.4 km in longitude. The time of each gridded image was assumed to correspond to the scan line that bisected that subsector of the full *GOES-8* image. Pixel brightnesses in each gridded image (range 0–255 units) were counted in five-unit bins to produce brightness frequency histograms, revealing a primary maximum from ground pixels and an extended upper tail caused by clouds. The median (peak) brightness of ground targets decreased with time after local solar noon, ranging from 75–80 units (83 units) at 1815 to 70–75 units (77 units) at 2015, and peak ground brightness values were below 80 units for all images presented in this study. Cloud brightness ranged from a minimum of about 80 units to a maximum of over 150 units. Discriminating cloud from ground pixels required a threshold, taken in this study as 80 units.

c. Photogrammetric analysis of ground-based digital cloud images

A series of 30-s interval time-lapse mini-DV format digital camera images were analyzed to obtain animations of the cumulus cloud-base field in the area of the 24 May deployment. The image aspect ratios were corrected for the 11:10 pixel aspect ratio of the mini-DV camera employed during IHOP. Radial distortion in-

troduced by a wide-angle lens was removed from the images using commercially available image processing software. Since the variable focal length of the mini-DV camera was not recorded, a 5 m × 2.5 m Cartesian grid was photographed with the camera at a variety of focal lengths. A calibration curve was developed between the known focal lengths and a radial distortion removal parameter. In processing IHOP images, distortion was iteratively removed until the horizon line matched an image overlay for 0° elevation angle (e.g., Rasmussen et al. 2003). Via the empirically derived relationship between the distortion parameter and the focal length, the actual focal length was then derived. The derived focal length value was confirmed in the 24 May case by examining the azimuthal difference between two distant landmarks with known ground locations in the image and the photograph. Following the techniques of Rasmussen et al. (2003), the image scaling uncertainty was estimated to be about 1%.

The time-lapse cloud field images are masked to identify cloud-base areas using a commercially available image-processing program. Since data are available from only a single camera in the chosen cases, an assumption of cloud-base height is required to determine the horizontal location of each cloud-base pixel (Rasmussen et al. 2003). In the 24 May case, the cloud-base height of roughly 1.8 km AGL is globally estimated using sounding data and the 3D Lagrangian analysis, and resulting cloud mappings are compared to GOES imagery to qualitatively validate the chosen cloud-base value. Assuming an uncertainty of ±100 m in cloud-base height, the expected range error of the single camera analysis is roughly ±400 m at a 15° elevation (Fig. 5). The number of cloud (N_c) and total (N_t) pixels in each grid cell are counted, and the ratio $R_c = N_c/N_t$ is stored at each grid point to complete the cloud analysis. A series of 30-s interval contour maps of cloud-base area on the radar analysis grid are generated assuming a threshold value of $R_c = 0.25$ (i.e., >25% cloud-base coverage in grid cell).

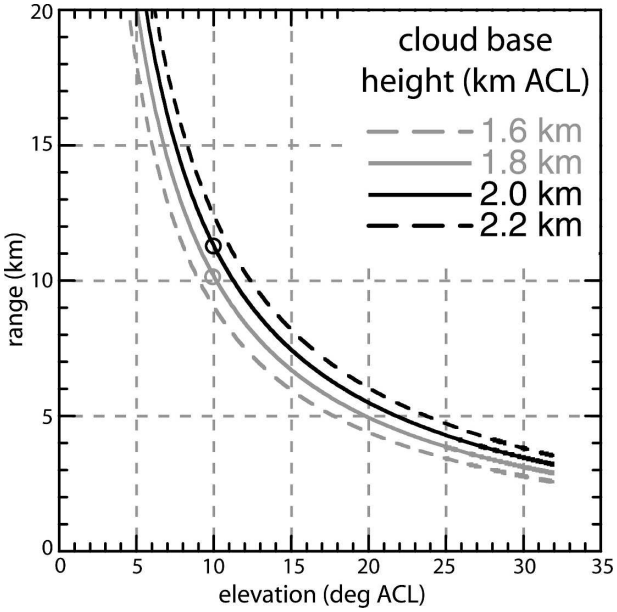

FIG. 5. Pixel horizontal range (km) as a function of image elevation angle (deg above horizontal plane through camera) for various assumed cloud-base heights [km above camera level (ACL)] for the single camera photogrammetric cloud field analysis.

4. Illustration of the Lagrangian analysis method

Different spatial and temporal Barnes smoothing parameters are employed in the 22 May and 24 May cases to reflect differing values of leg length and spacing of the mobile mesonets and differing wind speeds in the Lagrangian analyses (Table 1; Fig. 2). Employing an advective time scale $T = L_U/U$ and calculating T from a "target" minimum resolvable wavelength L_U (kilometers) and a leg-normal horizontal velocity scale U (meters per second), values of τ_L are selected to yield a second–pass response $R_2 = 0.05$ at the time scale T for each case (Table 1). Values of τ_i are selected that achieve $R_2 = 0.05$ at characteristic leg lengths of about 10 min, with a slightly larger τ_i value chosen on 24 May due to increased local evolution caused by the rapid motion of the CF (Table 1). Values of κ_s are selected that achieve $R_2 = 0.05$ at a characteristic horizontal wavelength L_h of 0.25 km (0.35 km) on 22 May (24 May), where L_h is roughly twice the analysis volume-averaged Lagrangian data spacing (Table 1). All observations within ±12 min (15 min) of the nominal analysis time are incorporated in the 22 May (24 May) analyses, corresponding to a 24-min (30-min) data window. The trajectory time duration value, which factors the effects of mean wind speed and horizontal ERL dimension, is 12 and 45 min in the 22 May and 24 May cases, respectively.

Many sensitivity tests were performed for each case study in which varying numbers of Lagrangian points and unique trajectories were required to calculate weighted gridpoint analysis values. The Barnes weighting of too small a number of independent trajectories and Lagrangian points tended to create analysis artifacts (e.g., extrapolation) as judged by visual inspection of output. To improve accuracy by assuring a representative sample of BL parcels from differing source air masses, at least 12 Lagrangian points from a minimum of three unique trajectories from different initial locations are required to calculate a weighted gridpoint

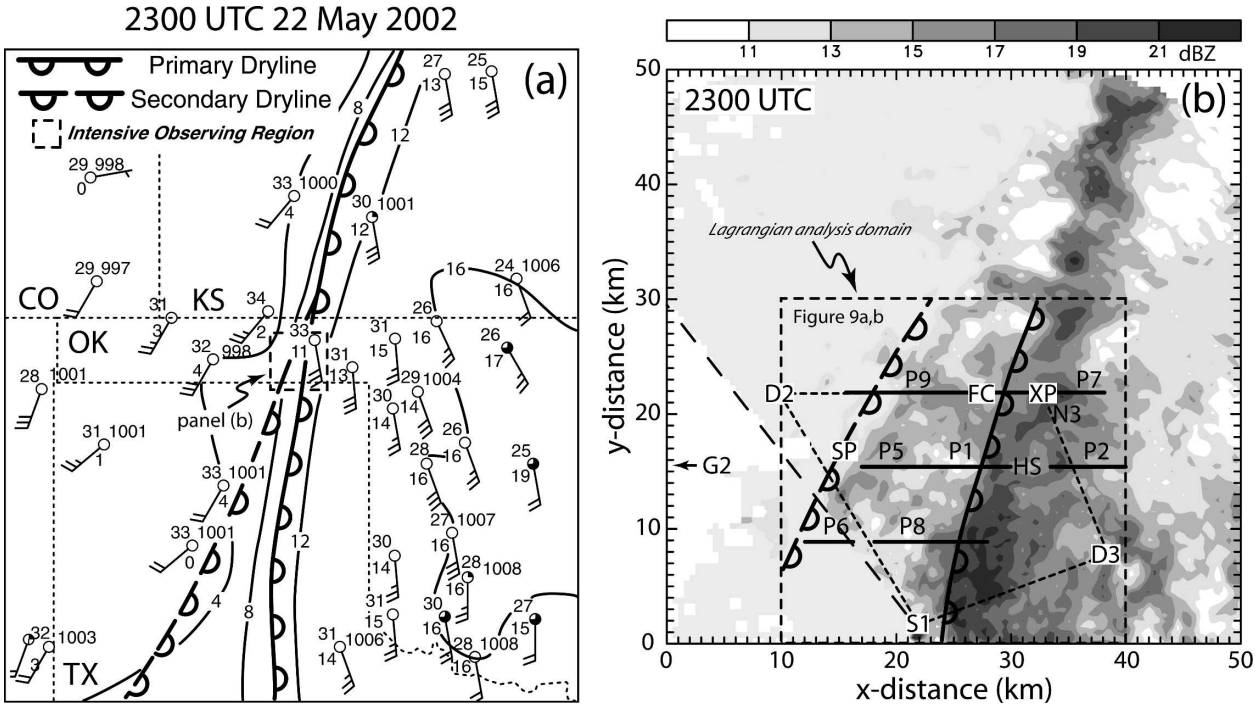

FIG. 6. Surface conditions and radar fields at 2300 UTC 22 May 2002. (a) Surface observations and IOR containing mobile radar and in situ measurements; (b) SR-1 radar reflectivity (dBZ) and surface platform locations. Surface station model includes temperature (°C) over dewpoint (°C) at left and mean sea level pressure (mb) at right, with a full wind barb equal to 5 m s^{-1} and a half barb equal to 2.5 m s^{-1}. In (b), "P1" through "P9" denote mobile mesonets, "S1" is SR-1, while "D2," "D3," and "XP" are DOW mobile Doppler radars, "G2" and "N3" are the mobile GLASS and CLASS sounding systems, respectively, "HS" is the fixed Homestead profiler site, and "FC" is the field coordination vehicle. The 2247 UTC G2 sounding (Figs. 4a,b) is located at (−6, 15). The figure is adapted from Buban et al. (2005).

value. Otherwise, the value from a reference sounding (described in section 2c) is assigned to that grid point.

a. 22 May 2002 dryline

A dryline was observed in the eastern Oklahoma panhandle by seven mobile mesonets, the KA and P-3 aircraft, the SR1 radar and the three DOW radars, and other mobile platforms on 22 May 2002 (Buban et al. 2005; Ziegler et al. 2004). The DL moved gradually eastward and became sharply defined during late afternoon (Fig. 6), then became quasi-stationary prior to retrograding westward during early evening. A few shallow, high-based cumuli developed along the DL, but CI did not occur. Because of favorably wide spacings of the mobile mesonet legs and strong winds, the Lagrangian analysis is performed on a 30 km × 30 km × 2.5 km subdomain. The grid-averaged number of Lagrangian points per trajectory and the number of independent trajectories per grid point are about 80 and 21, respectively (Table 2). The mobile in situ ground-based and aircraft observations for this case are analyzed in detail by Buban (2005) and Buban et al. (2007). Finescale observations using other sensors in

TABLE 2. Trajectory and Lagrangian point statistics of the 22 May and 24 May 2002 IHOP case studies. The calculation of the total Lagrangian points per case assumes 120 and 225 Lagrangian points per trajectory on 22 May and 24 May respectively (i.e., Lagrangian point interval of 6 s on 22 May and 12 s on 24 May). The quantities in the rightmost three columns are global estimates based on grid averages.

Case day	No. of trajectories (N_T)	No. of Lagrangian points (N_L)	No. of grid points (N_{GP})	Grid points per trajectory (N_{GT})	Lagrangian points per grid point (N_L/N_{GP})	Unique trajectories per grid point ($N_{GT} \times N_T/N_{GP}$)
22 May	2.2×10^4	2.6×10^6	4.1×10^4	40	63	21
24 May	1.9×10^4	4.3×10^6	2.9×10^4	20	148	13

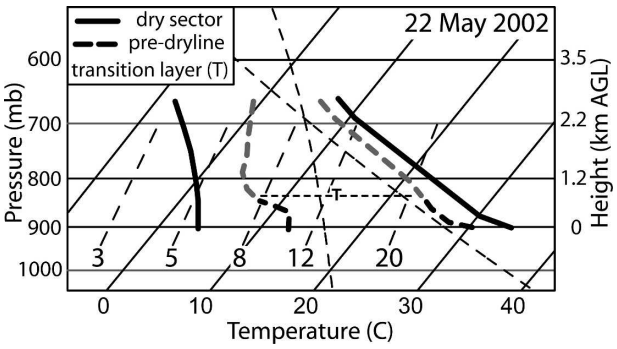

FIG. 7. Reference soundings displayed on a skew T–log p diagram for the 22 May 2002 dryline case (see also Fig. 4). The portion of the convective BLs (black) extending through the top of the domain in the dry sector sounding and through the transition layer in the pre-dryline sounding (depths of 2.5 and 0.75 km, respectively) are used only for grid-column soundings in the interior of the Lagrangian analysis domain. The portion of the pre-dryline sounding from the transition layer to the top of the sounding at 2.5 km is gray colored. The total sounding is used to specify grid-column soundings on lateral inflow boundaries only in the appropriate air mass.

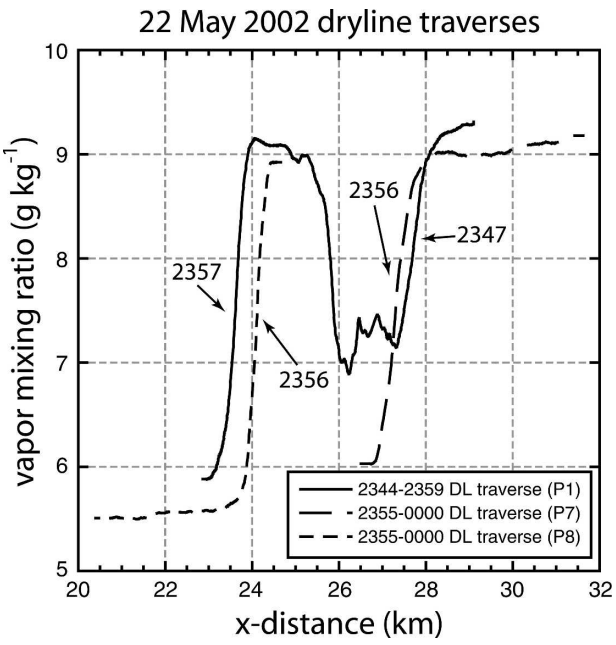

FIG. 8. Profiles of q_v (g kg^{-1}) on selected dryline traverses by mobile mesonets P1, P7, and P8 on 22 May 2002. Sharp, large-amplitude gradients locate the dryline transects at indicated midtransect times.

the same area on 22 May are reported by Fabry (2006), Weiss et al. (2006), and Demoz et al. (2006).

The reference soundings, composited from mobile and fixed site soundings and DL traverses executed by the mobile mesonets and the KA, reveal the warmer and drier BL west of the DL than to its east (Fig. 7; see also Fig. 4). A transition layer at 0.75 km separates the moist BL from an elevated residual layer (ERL) that is slightly cooler and moister than the deep dry layer to the west of the DL. Mobile mesonet traverses during early evening mark the DL by q_v gradients of order 3 g kg^{-1} per 0.5–1 km (Fig. 8). The southern leg defines a western DL segment, the northern leg defines an eastern DL segment, and the central leg locates both the western and eastern DL segments and a sharply defined west-to-east q_v decrease between the two DL segments.

The role of southerly along-DL flow and moisture advection in the Lagrangian analysis is to effectively extend the western and eastern DL segments between the adjacent traverses, which define their respective locations. The combination of strong southerly moisture advection with the complex moisture profile of the central traverse results in a finite-length moist tongue and an inflection of the surface DL (Fig. 9). Confluent horizontal trajectories and airflow at the DL (Figs. 9a,b) support the development of the observed across-DL moisture gradient (Fig. 9b) via convergent frontogenesis. BL moisture in the grid-column soundings (Fig. 9a) is redistributed along trajectories by the vertical DL-normal circulations (Figs. 9c,e) for subsequent grid-point interpolation. A complex local juxtaposition of trajectories with dry and moist BL origins produces quasi-homogeneous BLs on either side of the DL and a "mixing zone" in q_v and θ_v that is centered on the main secondary circulation (Figs. 9d,f; see also Ziegler and Hane 1993).

b. 24 May 2002 cold-frontal–dryline "triple point" intersection

The armada of mobile observing platforms was deployed in the vicinity of a rapidly southeastward-moving cold front and its "triple point" dryline intersection west of Shamrock, Texas, in the eastern Texas panhandle on 24 May 2002 (Ziegler et al. 2003, 2004). Despite the development of a dense cumulus field to the east of the CF and DL (Fig. 10a) and deep convective potential based on early forecast soundings, CI did not occur near the triple point. However, storms developed from west Texas northeastward into western Oklahoma to form a squall-line mesoscale convective system (MCS; Fig. 10b). Due to lighter winds and a more irregular spacing of the mobile mesonet legs than in the 22 May case, the Lagrangian analysis is performed on a 25 km × 25 km × 2.5 km subdomain. The grid-averaged number of Lagrangian points per trajectory and the number of independent trajectories per grid point were about 100 and 13, respectively (Table 2). A detailed analysis of the BL and cumulus forma-

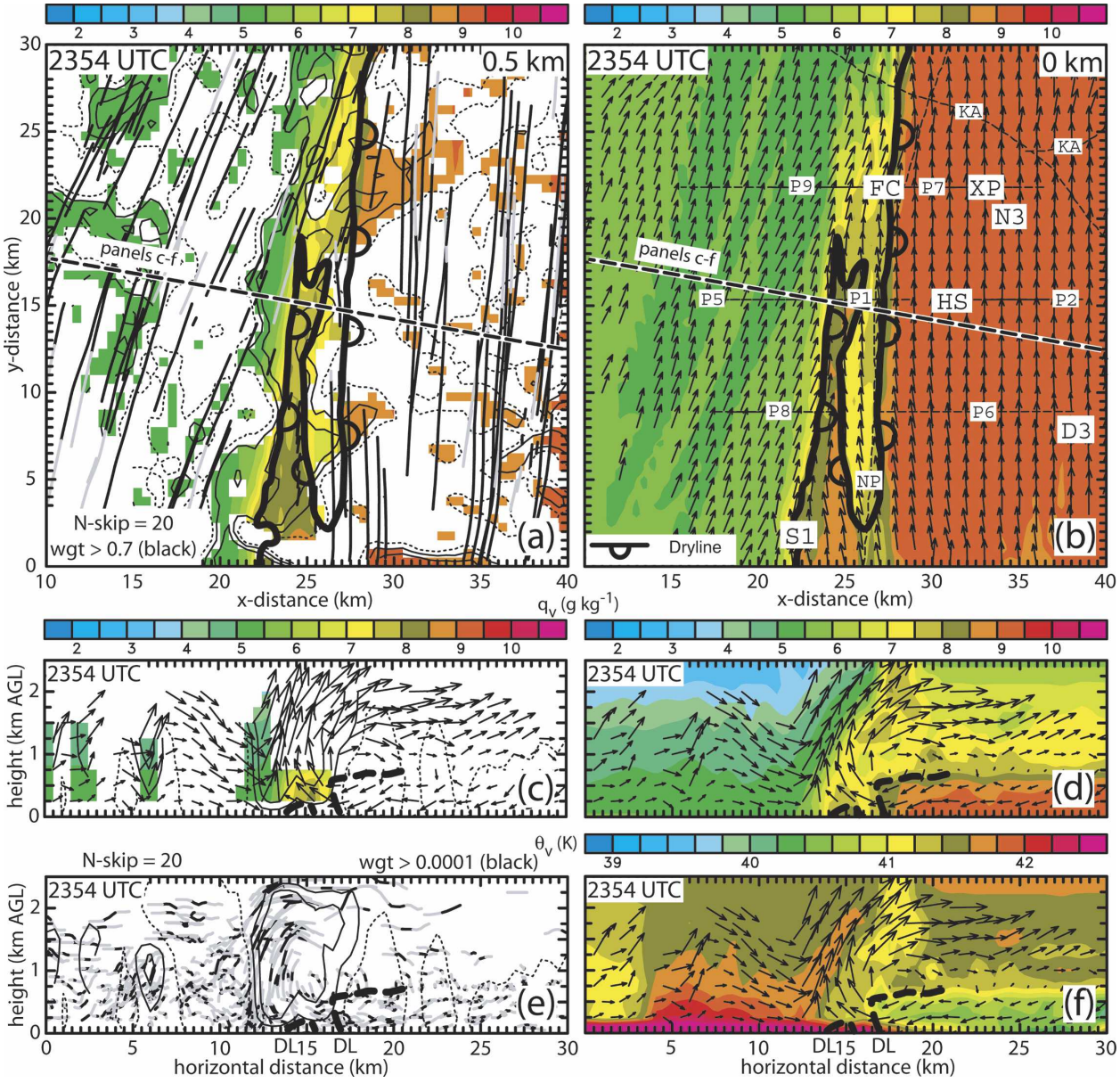

FIG. 9. Lagrangian analysis fields at 2354 UTC 22 May 2002. (a) Selected gridpoint air trajectories (every 20th trajectory), vertical velocity, and q_v (g kg^{-1}) of grid-column soundings at 0.5 km; (b) vector horizontal ground-relative velocity (every other grid point with 1-km vector length equal to 15 m s^{-1}) and Lagrangian analysis of q_v (g kg^{-1}) at ground level; (c) vertical cross section containing q_v (g kg^{-1}) of grid-column soundings and vector ground-relative velocity (1-km vector length equal to 5 m s^{-1}) in the cross section; (d) vertical cross section of Lagrangian analysis of q_v (g kg^{-1}) with vector ground-relative flow; (e) vertical cross section locating selected grid-column trajectories passing through or near that cross section, with black fill denoting the product of Lagrangian time and spatial weights > 0.0001 (every 20th trajectory); (f) vertical cross section of Lagrangian analysis of θ_v (°C) with vector ground-relative flow. The cross section is located in (a) and (b). Vertical velocity in (a), (c), and (e) is contoured at an interval of 1 m s^{-1} starting at 0.5 m s^{-1} (thin black curve), while a dotted curve indicates $w = 0$ m s^{-1}. In (b), "KA" and "NP" denote the King Air and P-3 aircraft, respectively, while other labels are defined in the Fig. 6 caption.

tion with these mobile ground-based and aircraft observations is described by Ziegler et al. (2007). Other finescale observational analyses of the CF and DL are presented by Wakimoto et al. (2006) and Geerts et al. (2006).

The reference soundings on 24 May reveal the warmer and drier BL west of the DL than to its east (Fig. 11; see also Fig. 4). A transition layer at 1.25 km separates the moist BL from an ERL that is slightly cooler and moister than the deeper, drier layer to the

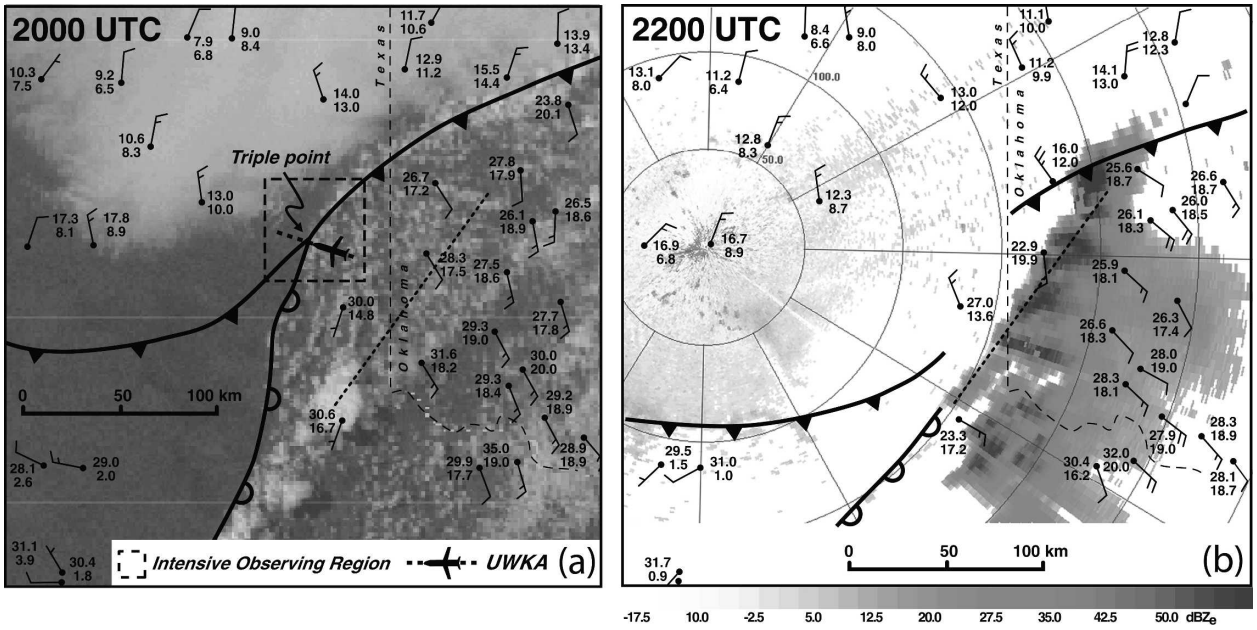

FIG. 10. Surface conditions, cloud cover, and radar fields during midafternoon on 24 May 2002. (a) Visible satellite image, surface observations, KA aircraft track, and IOR containing mobile radar and in situ measurements at 2000 UTC; (b) Weather Surveillance Radar-1988 Doppler (WSR-88D) radar reflectivity composite from Amarillo, TX, and surface observations at 2200 UTC. Surface station model includes temperature (°C) over dewpoint (°C), with a full wind barb equal to 5 m s^{-1} and a half barb equal to 2.5 m s^{-1}. The figure is adapted from Wakimoto et al. (2006).

west of the DL. In contrast, a second transition layer at 1.75 km separates the deep, dry BL west of the DL from an overlying, very dry ERL. The ERL top to the east of the DL is at 2 km, suggesting a process whereby

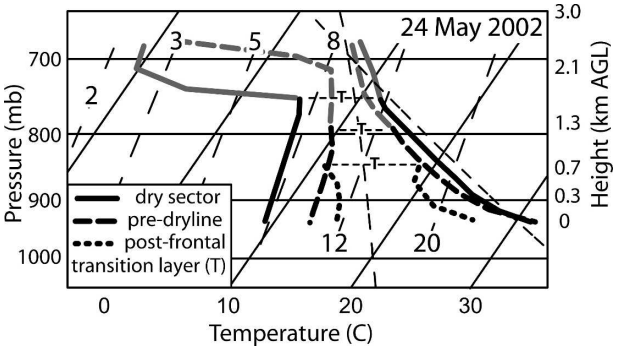

FIG. 11. Reference soundings displayed on a skew T–log p diagram for the 24 May 2002 dryline case (see also Fig. 4). The portions of the soundings (black) extending from the surface through the transition layers of the postfrontal, dry sector, and pre-dryline convective BLs (depths of 0.75, 1.75, and 1.25 km, respectively) are used for grid-column soundings only in the interior of the Lagrangian analysis domain. The portion of the soundings from the transition layer to the top of the sounding at 2.5 km is gray colored. The total sounding is used to specify grid-column soundings on lateral inflow boundaries only in the appropriate air mass. The portion of the postfrontal sounding above the transition layer (which is the same as the dry sector sounding) has been omitted for clarity.

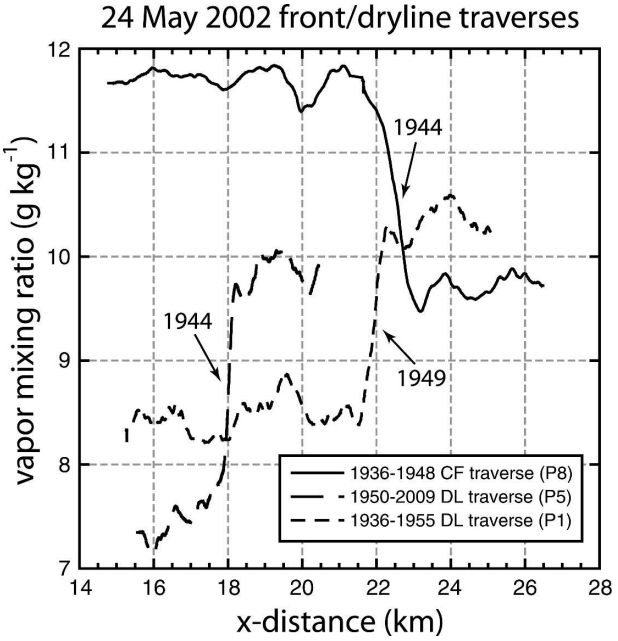

FIG. 12. Profiles of q_v (g kg^{-1}) on selected cold-frontal and dryline traverses by mobile mesonets P1, P5, and P8 on 24 May 2002. Sharp, large-amplitude gradients locate the cold front (P8) and dryline (P1, P5) at indicated midtransect times.

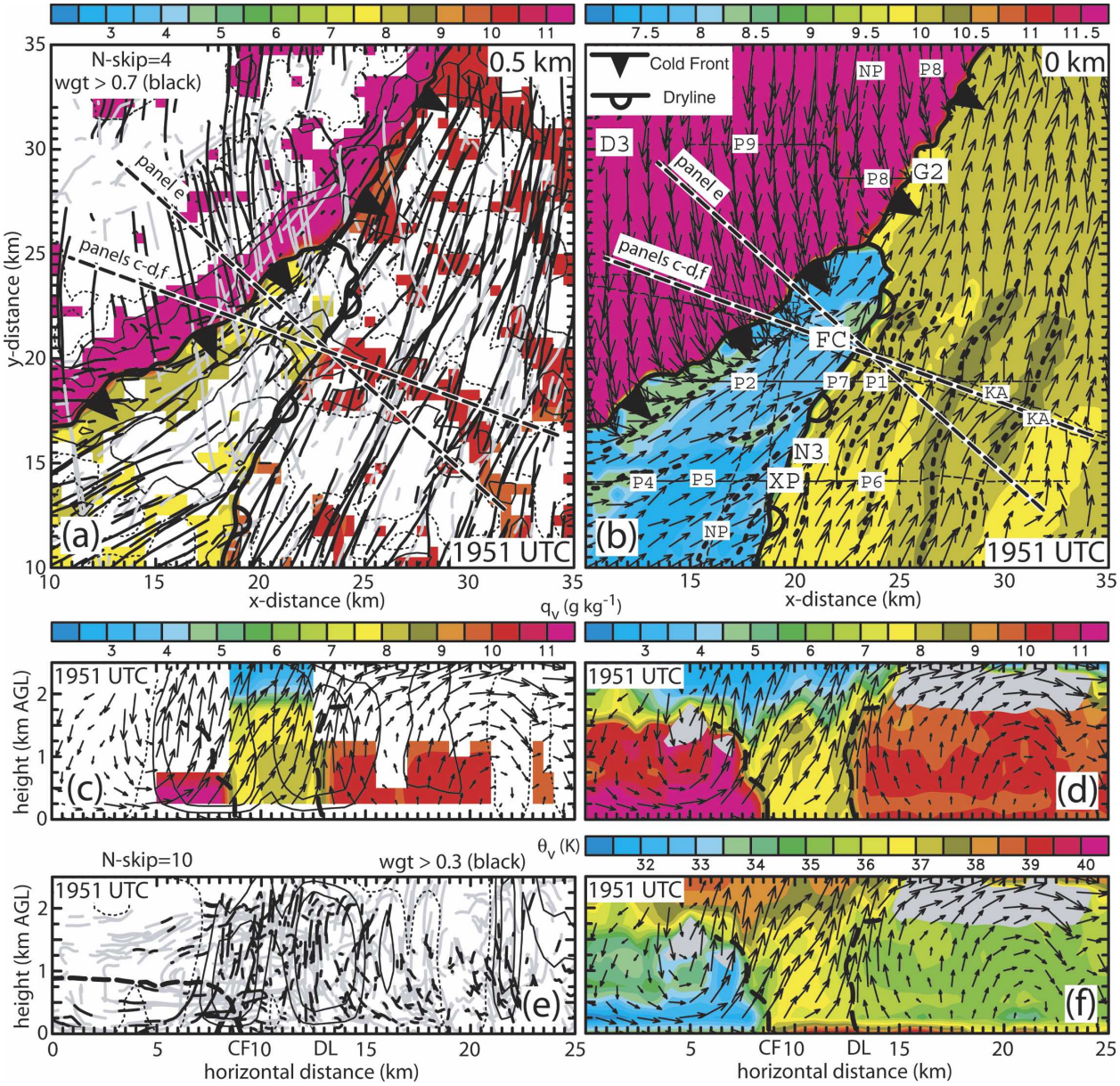

FIG. 13. Lagrangian analysis fields at 1951 UTC 24 May 2002. (a) Selected gridpoint trajectories (every 4th trajectory) and q_v (g kg^{-1}) of grid-column soundings at 0.5 km; (b) vector horizontal ground-relative velocity (every other grid point with 1-km vector length equal to 4 m s^{-1}) and Lagrangian analysis of q_v (g kg^{-1}) at ground level; (c) vertical cross section containing q_v (g kg^{-1}) of grid-column soundings and vector ground-relative velocity (1-km vector length equal to 5 m s^{-1}) in the cross section; (d) vertical cross section of Lagrangian analysis of q_v (g kg^{-1}) with vector ground-relative flow and gray-filled water-saturated areas (i.e., may be inferred as cloud); (e) vertical cross section locating selected grid-column trajectories (every 10th trajectory) passing through or near that cross section, with black fill denoting the product of Lagrangian time and spatial weights > 0.3; (f) vertical cross section of Lagrangian analysis of θ_v (°C) with vector ground-relative flow and gray-filled cloud. Note differing color-fill scales in (a), (c), and (d) vs (b). Cross sections are located in (a) and (b). Vertical velocity in (a), (c), and (e) is contoured at a 1 m s^{-1} interval starting at 0.5 m s^{-1} (thin black curve), while a dotted curve indicates $w = 0$ m s^{-1}. Labels are defined in the captions of Figs. 6 and 9.

the overlying, very dry ERL has been lifted as westerly flow crosses the DL. A third transition layer at 0.75 km separates the postfrontal BL from an overlying ERL formed by advection of the deep, dry layer from front-to-rear relative to the advancing surface CF. Mobile mesonet traverses during midafternoon mark the DL and CF by q_v gradients of order 2 g kg^{-1} per 0.5 km and 2 g kg^{-1} per 1 km, respectively (Fig. 12), including the typical "single step" profile also commonly observed in the 22 May case.

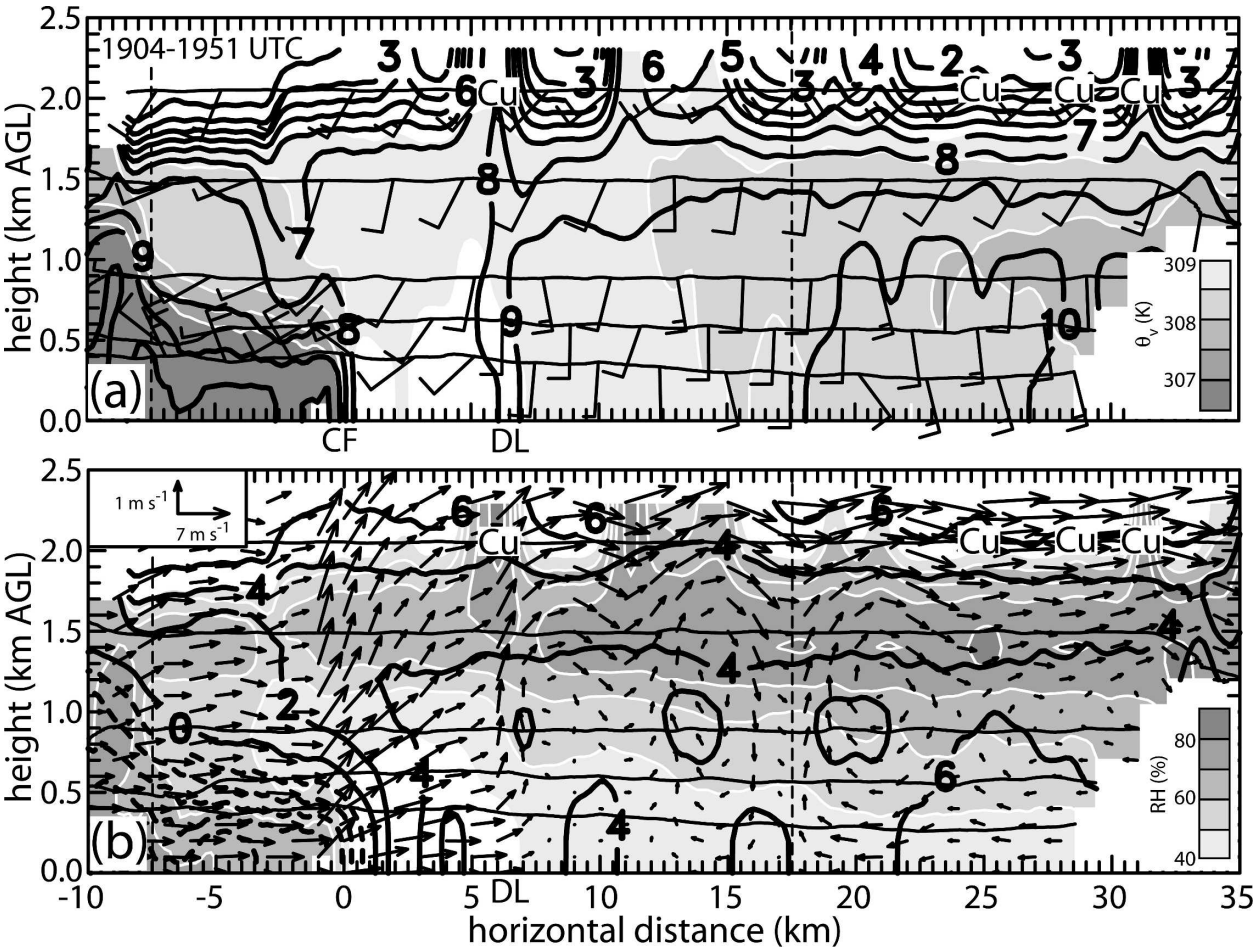

FIG. 14. 2D objective analysis of KA stepped traverse measurements in the period 1904–1951 UTC 24 May 2002. The KA objective analysis is located in a vertical WNW–ESE cross section that approximately contains the KA legs and coincides with the Lagrangian analysis cross sections in Figs. 13c, 13d, and 13f. The fine vertical dashed lines locate the lateral boundaries of the cross sections in Figs. 13c, 13d, and 13f. (a) Vapor mixing ratio (black contours at 1 g kg^{-1} interval), gray-filled virtual potential temperature (K), and horizontal wind barbs (full barb = 5 m s^{-1}, half barb = 2.5 m s^{-1}); (b) vector air velocity in the cross section (scaled at upper left), normal horizontal airspeed into the plane (black contours at 2 m s^{-1} interval), and gray-filled relative humidity (%). Compare fields in (a) and vectors in (b) to Figs. 13d and 13f. Symbol "Cu" = "cumulus" recorded by the forward video camera on the KA.

The Lagrangian analysis near the time of the mobile mesonet traverses reveals the sharply defined DL and CF (Fig. 13). The ubiquitous pattern of confluent horizontal trajectories marking both boundaries (Fig. 13a) provides frontogenetic support of the observed across-boundary moisture gradients (Fig. 13b). The single-step moisture profiles observed by P1 and P5 (Fig. 12) produce a simpler DL orientation than on 22 May (Fig. 13b

→

FIG. 15. Water-saturated areas from Lagrangian analysis (i.e., cloud fields), *GOES-8* visible imagery, and digital camera cloud base outline analysis at 1.75 km on 24 May 2002. The radar, satellite, and cloud-base analyses are performed in the larger area while the Lagrangian analysis is restricted to the subdomain bordered by fine dashed lines. All panels also show horizontal and vertical velocities. (a) Lagrangian relative humidity (%) at 1906 UTC, with overlaid "satellite view" of vertically integrated cloud cover (i.e., height $Z > Z_{LCL}$) at any level in each grid column (gray filled) and cloud depth ≥0.3 km (white); (b) *GOES-8* visible image brightness > 80 units (0–255 scale) at 1906 UTC; (c) as in (a) but including area of >25% cloud-base coverage from digital camera analysis (heavy black curve) at 1924 UTC; (d) as in (c) but at 1933 UTC; (e) as in (c) but at 1942 UTC; (f) *GOES-8* cloud area as in (b) with cloud-base outline as in (c) at 1942 UTC. Thin, long-dashed lines denote the azimuthal sector and the central 260° azimuth viewed by the digital cloud camera ("C1"). Magnitude of horizontal velocity vector is scaled by 1 km = 10 m s^{-1}. Vertical velocity is contoured at an interval of 1 m s^{-1} starting at 0.5 m s^{-1} (thin black curve), while a dotted curve indicates $w = 0$ m s^{-1}. White-filled circles locate updraft cores in all panels. Color-bar label "ib" denotes satellite "image brightness" scale.

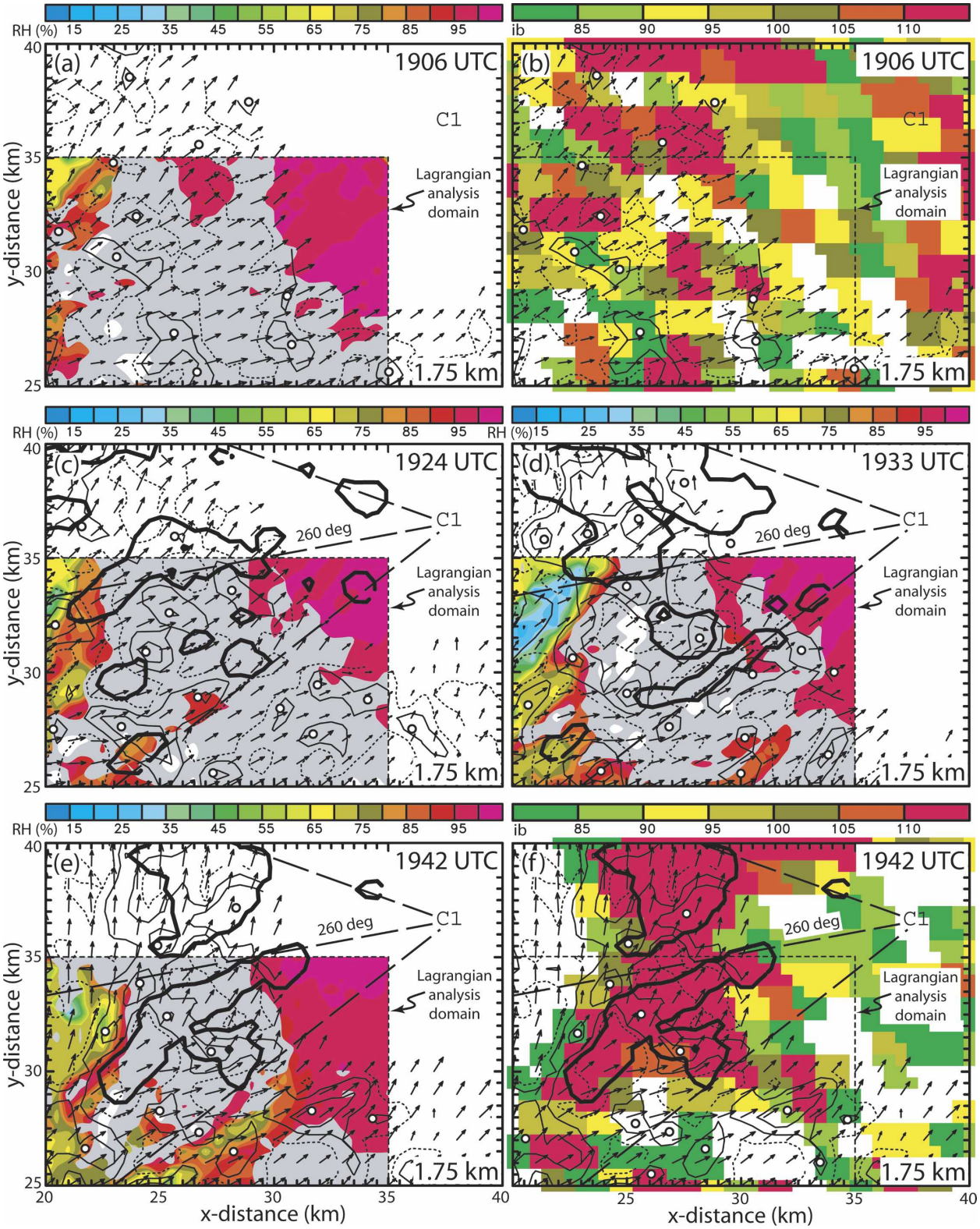

versus Fig. 9b). The CF displays a more undulating form than the DL due to large alongfront variations in shear, local circulations, and frontogenesis. Grid-column soundings provide a source of BL moisture (Fig. 13a) that is redistributed by the vertical CF- and DL-normal circulations and along-boundary shear (Figs. 13c–f) for subsequent gridpoint interpolation. A deep, erect zone of confluence with weak DL-normal shear in the vertical plane maintains a narrow mixing zone above the DL aloft (Figs. 13d–f), in contrast with the relatively broad mixing zone in the 22 May case (Figs. 9d–f).

Observations from the stepped traverse pattern conducted by the KA in the period 1904–51 (oriented as in Fig. 10a) define a roughly 6-km-wide, rather homogeneous, dry convective BL between the CF and DL (Fig. 14). The KA stepped traverse analysis is consistent with the Lagrangian analysis (Figs. 13d,f), the latter assimilating KA data from only portions of the lowest three legs. Since the relative CF and DL motion speeds could not be considered, the structure of the frontal head is not well resolved in the (DL relative) stepped traverse analysis due to the ~30 min time difference between the midlevel and near-surface legs. Horizontal gradients of moisture and horizontal wind clearly delineate the CF and DL, with sharply colder and moister postfrontal air (Fig. 14a versus Figs. 13d,f). As indicated by the multiple moist BL legs, a sustained westward-directed virtual temperature gradient east of the DL provides solenoidal forcing to promote backing BL winds and westerly shear (Figs. 14a,b). The θ_v field in the moist BL east of the DL is rather inhomogeneous, the moist BL is slightly cooler than the BL west of the DL, and the lowest 500–1000-m layer of the moist BL is weakly unstable (Fig. 14a versus Fig. 13f). Vertical motion is concentrated in maxima along the DL and CF (Fig. 14b versus Figs. 13a,c–f). Although BL rolls with ~5 km spacings are inferred to the east of the DL (Fig. 14b) in agreement with the radar analysis, vertical motions in the KA cross-sectional objective analysis are considerably weaker than Doppler analysis values. A plume of high q_v values above the surface DL location feeds the base of a deep developing cumulus cloud whose northern flank was penetrated by the KA at around 1910 on its highest leg (Fig. 14a). Shallower cumulus tops are penetrated by the KA on the eastern end of its highest leg. The bases of all observed cumuli are above the 1.5-km leg near the top of a layer of high relative humidity locally exceeding 80%.

Results demonstrate internal consistency between evolving cloud cover analyses from *GOES-8* imagery, the digital cloud camera, and the Lagrangian data. Given the sparse in situ data and Lagrangian OA assumptions, the water-saturated areas are reasonably consistent with satellite cloud tops (Figs. 15a,b,e,f) and measured cloud bases (Figs. 15c–e). Individual cloud-base centers move with the subcloud winds and are located either in or on the downstream edge of updraft cores (Figs. 15b–d). Roughly 50% of the cloud-base areas are actively forced [i.e., situated in updraft below the LFC as defined by Stull (1985)], while some clouds bases deactivate as they advect downstream to form along-flow moisture plumes. Drier air advects into and progressively erodes the western edge of the cloudy region in both the Lagrangian analysis and cloud observations.

The cumulus area and large subcloud vapor mixing ratio values are concentrated in the moist sector ahead of the CF and DL at 1951 (Figs. 16a,b versus Fig. 13b). Other small clouds are located immediately behind the front (Figs. 16a,b) and are forced by lifting of cool, moist air by postfrontal updraft plumes (Figs. 13d,f). As at earlier times, there is good internal consistency between evolving cloud cover analyses from *GOES-8* imagery, the digital cloud camera, and the Lagrangian data (Figs. 16c,d). The large heterogeneity of subcloud relative humidity (Fig. 16b) is forced by mesoscale moisture fluxes caused by the complex, evolving updraft field and the gridpoint Lagrangian OA of parcels with widely varying BL origin locations and airmass characteristics. This "mesoscale mixing" process and the resulting heterogeneous pattern of water saturation produce a complex cloud field to the east of the DL (Fig. 16b).

5. Conclusions

This paper reports the development and application of a new Lagrangian analysis technique that assimilates and fills data voids in BL in situ measurements by distributing these observations along trajectories defined by time-varying 3D multiple radar analyses and interpolating these Lagrangian data to the grid used for the radar analysis. The method is illustrated in the 22 May DL and 24 May CF–DL triple point cases during IHOP. Analyses of in situ data from mobile mesonets, aircraft, and sounding systems define the finescale gradients and evolution of moisture and virtual potential temperature delineating the 22 May and 24 May DLs, the 24 May CF, and the complex BL morphology. The Lagrangian analysis technique provides high-resolution output fields of water vapor mixing ratio, potential temperature, and virtual potential temperature, from which key parcel parameters including the lifting condensation level and the level of free convection are readily de-

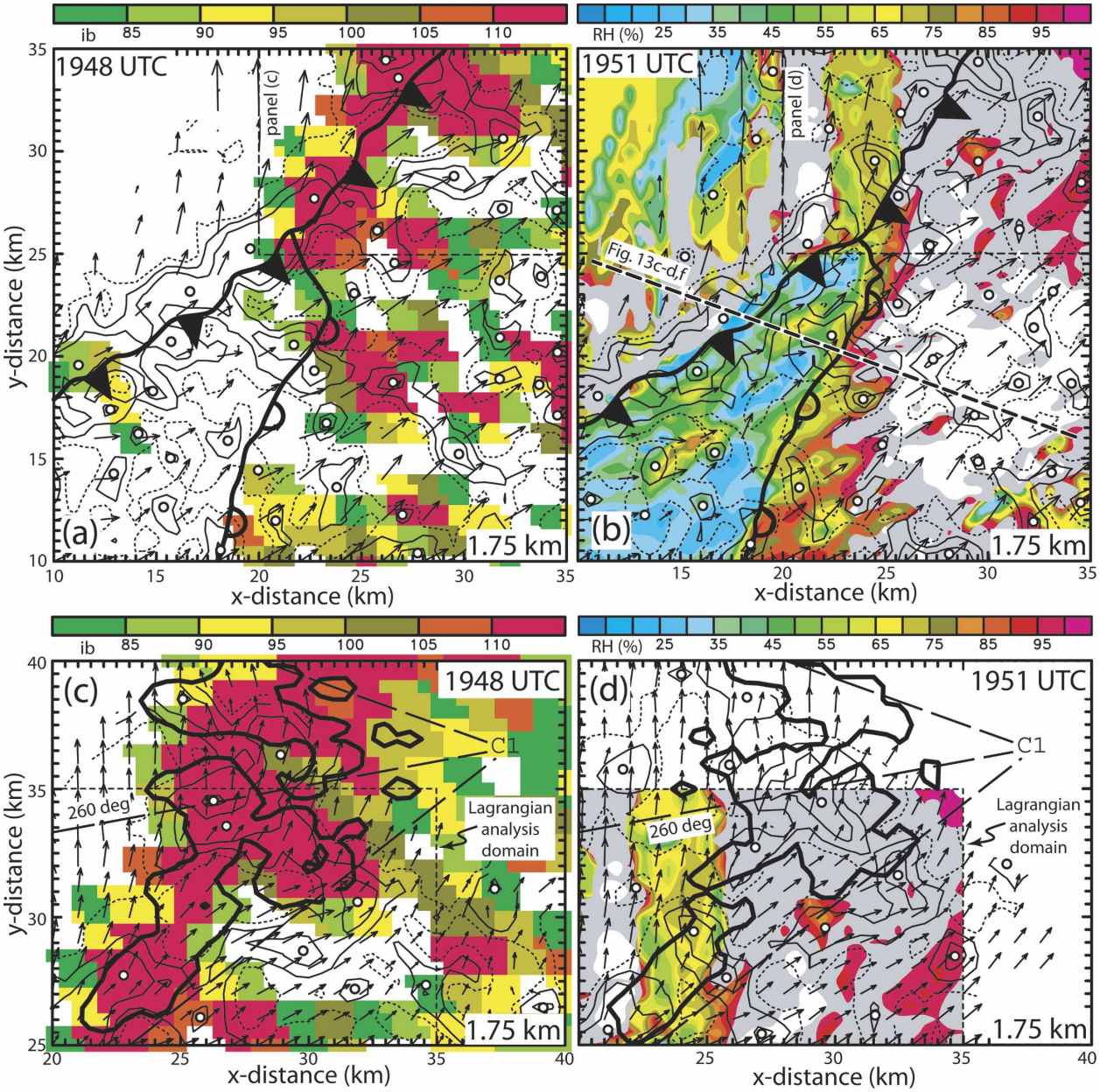

FIG. 16. Comparison of cloud fields from gridded digital camera, *GOES-8* visible imagery, and Lagrangian analysis at 1.75 km on 24 May 2002. (a)–(d) Show horizontal and vertical velocities. (a) *GOES-8* imagery at 1948 UTC; (b) Lagrangian cloud cover and relative humidity (%) over full Lagrangian analysis domain at 1951 UTC; (c) *GOES-8* imagery in same subdomain as in Figs. 15b and 15f, but at 1948 UTC; (d) as in Figs. 15a and 15c–e, but at 1951 UTC. Every other horizontal velocity vector is plotted with magnitude scaled by 1 km = 10 m s^{-1}. Thin solid contours denote positive vertical velocity at a 1 m s^{-1} contour interval starting at 1 m s^{-1}, while the dotted contour is zero vertical velocity. Positions of the surface cold front and dryline are inferred from the Lagrangian and radar analyses. Thin, long-dashed lines denote the azimuthal sector and the central 260° azimuth viewed by the digital cloud camera ("C1"). The thick dashed line locates vertical cross sections described in the text. White-filled circles locate updraft cores in all panels. Color-bar label "ib" denotes satellite "image brightness" scale.

rived. The patterns of relative humidity and water saturation from the Lagrangian analysis—and by inference the cumulus field—are reasonably consistent with *GOES-8* visible imagery and single-camera photogrammetric cloud base analyses, indicating that the Lagrangian analysis method has the potential to assist in defining the boundary layer cumulus formation and CI processes.

Acknowledgments. We thank the numerous individuals whose collective efforts made IHOP a success. The assistance of Robert Rabin with the McIDAS analysis of satellite imagery is gratefully acknowledged. The insightful comments provided by Tammy Weckwerth and two anonymous reviewers helped to improve the manuscript. Primary funding for deploying NSSL's IHOP mobile facilities and for data analysis was provided under NSF Grant ATM-0130316. Yvette Richardson (PSU) provided the DOW radar data and consultation on radar analyses used in this study via NSF Grant ATM-0208651. Other funding to fabricate and deploy NSSL's mobile facilities for IHOP and to analyze IHOP data was granted by the High Performance Computing Consortium (HPCC), the United States Weather Research Program (USWRP), and the National Severe Storms Laboratory Director's Discretionary Fund (all NOAA agencies).

APPENDIX

Summary and Discussion of Lagrangian Analysis Algorithm

The Lagrangian analysis proceeds according to a multistep algorithm (Fig. A1). The following discussion synthesizes the discussion in the text with additional details of the multiple analysis steps (see also section 2 and Figs. 3 and 4).

a. Step 1: Precondition 4D winds and input in situ data

The series of all input multiple-Doppler radar analyses within the time window (Fig. A1, step 1a) are preconditioned with a velocity hole-filling procedure (Fig. A1, step 1b) to eliminate small data voids due to weak radar return that are sometimes present near the top and lateral peripheries of the wind analysis domain. As illustrated by wind and Lagrangian analysis results presented in the text, the wind hole-filling only permits a few high-altitude trajectories to extend into the elevated wind data voids. Wind hole-filling theoretically improves reliability of output fields near the analysis boundaries by providing boundary conditions, thereby mitigating extrapolation errors in the interior of the data-bearing volume (Achtemeier 1986). Missing horizontal wind component values are estimated by a weighted average of nearby points approximating an elliptic filter response. Mean winds are computed at each level from all available nonmissing points—including both observed and weighted-average values—and these mean wind values are substituted for all remaining missing values at a given level. Missing vertical air velocity values are simply set to zero, although the hole-filling algorithm could optionally be extended to treat the vector air velocity.

The airmass-dependent reference sounding profiles of height, pressure, q_v, θ, and θ_v are derived by compositing all available in situ sounding and aircraft observations within a given air mass at the prescribed analysis grid levels (Fig. A1, step 1c). The lowest ~250 m of a reference sounding is adjusted for consistency with ensembled surface mobile mesonet observations in the appropriate air mass.

In situ mobile mesonet and aircraft time series and sounding observations within the specified time window are prefiltered (Fig. A1, step 1d) to damp subgrid-scale variability (Mohr et al. 1986), then subsampled or decimated (Fig. A1, step 1e) to reduce correlation between successive filtered-decimated observations. Mobile mesonet measurements should be particularly sensitive to small-scale surface layer variability forced by land use and soil moisture changes (e.g., Segal and Arritt 1992), which nevertheless are not resolved by the Lagrangian analysis. Thus, prefiltering in situ data mitigates errors due to aliasing of unresolved scales. The mobile mesonet, aircraft, and sounding time series data are smoothed using a four-pass application of a triangular weighting function with a half-width of 12 s (e.g., Ziegler and Rasmussen 1998). The in situ data from the mobile mesonets (~15–25 m s^{-1} nominal road speed), M-GLASS soundings (~5 m s^{-1} rise rate), and aircraft (~100 m s^{-1} cruise speed) are then decimated at intervals of 6, 10, and 2 s, respectively, yielding effective along-track spacings of the decimated data of about 90–150, 50, and 150–200 m, respectively. The M-CLASS sounding data are retained at their full resolution (10 s). The latter effective data spacings regularize the spatial in situ data density for the subsequent 3D objective analysis to the radar grid, providing roughly three–five data points per grid interval in the traverse direction. The reader should note that any available remote measurements of vapor mixing ratio (e.g., DIAL lidar) and virtual potential temperature could also be incorporated into the Lagrangian analysis, the remotely sensed data at radar gate locations also being prefiltered and decimated.

b. Step 2: Distribute in situ data along 3D air trajectories

Following calculation of upstream and downstream air trajectories from each in situ datum location, trajectories are decimated to make the spacing of the Lagrangian data equivalent to the spacing of the initial (in situ) data points (Fig. A1, step 2a; Fig. 3). Equalizing the spacings of trajectory initial points and Lagrangian data makes the overall spatial data distribution more homogeneous (at least locally) and thus better suited to the spatial filter being employed

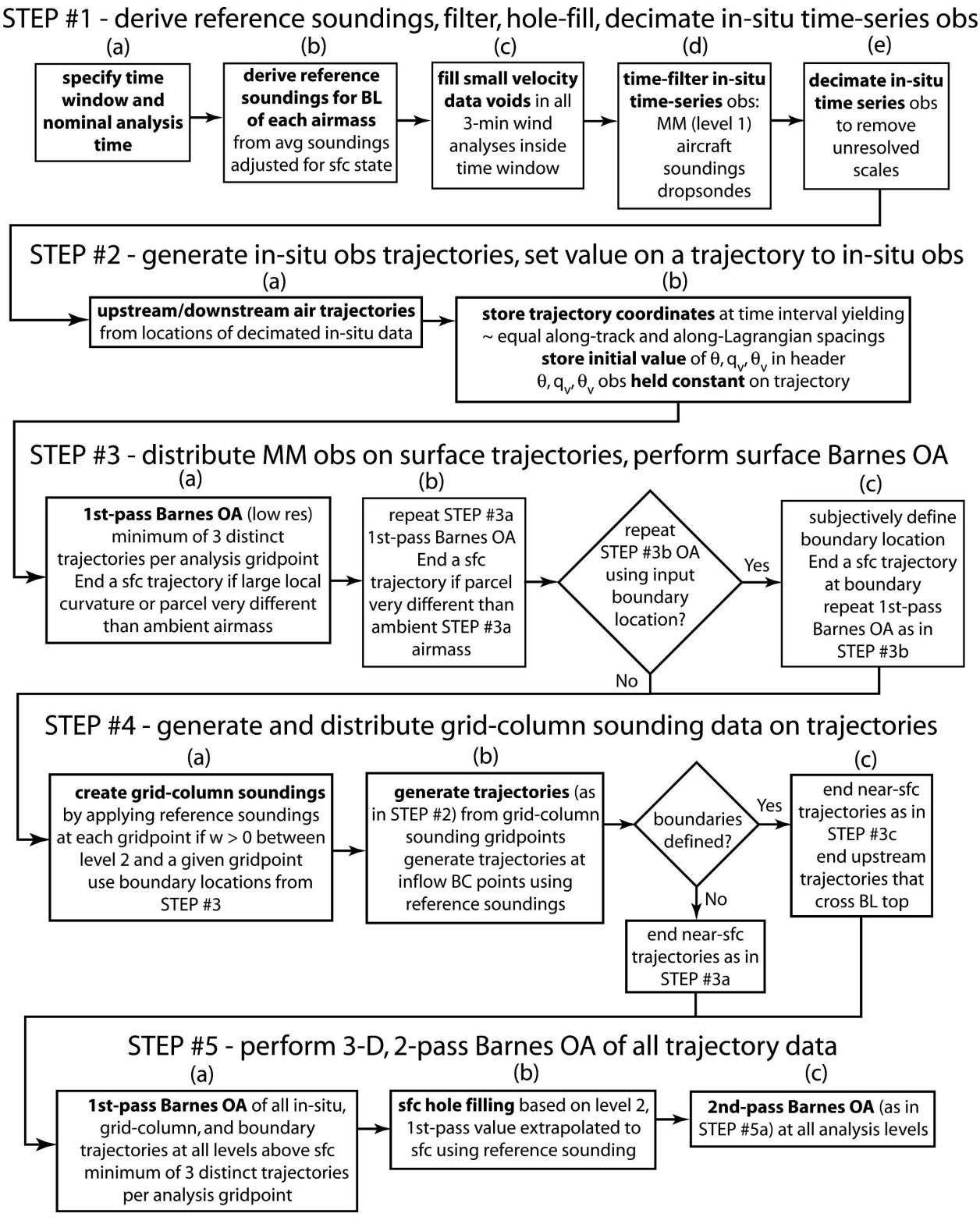

FIG. A1. Flow diagram illustrating the five-step Lagrangian objective analysis algorithm. Numbered main steps and substeps (a)–(e) are discussed in the text.

(Barnes 1994). The chosen 6 s (12 s) decimation interval in the 22 May (24 May) case compensates for differing horizontal air velocity scales and thus provides broadly comparable along-trajectory and along-leg data spacings (Fig. A1, step 2b).

c. Step 3: Perform 2D, surface Barnes objective analysis of mobile mesonet Lagrangian data

Although surface boundaries may move within the time window, they are analyzed relative to their nominal analysis time locations. Since convergent frontogenesis maintains CFs (e.g., Sanders 1955) and DLs (e.g., Buban et al. 2007; Ziegler et al. 1995), trajectory confluence is ordinarily sufficient to locate boundaries in the surface Lagrangian data. However, radar analysis errors due to poor low-level sampling (see section 2a) or the chance encounter of a mesovortex along a boundary may allow a few surface trajectories to cross the actual boundary. Additionally, since trajectories relative to a moving boundary are ground relative (i.e., not boundary relative and thus not subject to convergent frontogenesis at the nominal boundary location), a few of these trajectories may need to be truncated if they cross the nominal boundary position.

Prior to the interpolation of mobile mesonet Lagrangian data to the surface analysis grid, a series of parametric tests reflecting the above ideas are applied to detect and truncate any "boundary crossing" trajectories at the inferred boundary locations. The first three tests are imposed to flag boundary crossings that any single test might fail to detect (Fig. A1, step 3a):

1) The first test truncates a trajectory if its current Lagrangian point location deviates from a linear least squares fit of the previous Lagrangian points on that trajectory by more than 150 m. This test effectively stops all front-crossing trajectories and most DL-crossing trajectories.
2) The second test terminates trajectories moving into the wrong air mass relative to the nominal analysis time due to boundary movement.

The truncated trajectories are interpolated with a provisional smoothing pass of the Barnes weighting function (Fig. A1, step 3b). Proceeding from this provisional surface analysis, the third test truncates any trajectory whose initial vapor mixing ratio value differs from the provisional surface analysis value at any Lagrangian point by more than 2.0 g kg^{-1}. The trajectories satisfying tests 1–2 are then retruncated using the step 3b analysis and parametric test 3, followed by repeating the step 3b analysis (Fig. A1, step 3c).

A fourth test is employed in the 24 May case to truncate a very small number of residual boundary-crossing trajectories that approach the CF or a southeast–northwest-oriented DL segment at a large incidence angle and are missed by the previous three tests. The curves $C(y)$ and $D(y)$, which contain the x coordinates of the CF and DL respectively, are defined from the step 3c surface analysis fields. Objective analysis is restricted to those Lagrangian data located within the appropriate air mass whose initial conditions satisfy the following thresholds: 9–10.5 g kg^{-1} (pre-DL), $<$8.5 g kg^{-1} and $\theta_v > 310$ K (dry sector), and $>$10 g kg^{-1} and $\theta_v < 309$ K (postfrontal). The Barnes surface analysis is then repeated with the truncated trajectories (Fig. A1, step 3d).

d. Step 4: Generate 3D trajectories from boundary layer reference soundings

With the 2D surface objective analysis complete, the airmass-dependent reference soundings are used to prescribe grid-column soundings that in turn initialize 3D boundary layer trajectories (Fig. A1, step 4a; Fig. 3). Upstream and downstream trajectories are computed from each grid point in the grid-column soundings (Fig. A1, step 4b). If a surface analysis value is missing, the reference sounding value is used at all levels without adjustment for local surface conditions. Inflow lateral boundaries are treated as interior grid columns, except that only downstream trajectories are computed. Truncation checks are applied to all gridpoint trajectories to restrict them to the appropriate air mass (Fig. A1, step 4c).

e. Step 5: Perform 3D, two-pass Barnes objective analysis of all Lagrangian data

The 3D Barnes objective analysis smoothing (i.e., first) pass interpolates the mobile mesonet, aircraft, mobile sounding, and reference sounding gridpoint trajectories between 0.25 and 2.5 km (Fig. A1, step 5a; Fig. 3). A simple surface hole-filling procedure is applied using the first-pass 3D analysis fields (Fig. A1, step 5b). If a surface analysis value is missing but a value is present at the same (x, y) coordinates at 0.25 km, the value at the surface is replaced with the 0.25 km value minus a lapse rate computed from the airmass reference sounding. The 3D correcting (i.e., second) pass of the Barnes analysis is performed at all levels to complete the Lagrangian analysis (Fig. A1, step 5c).

REFERENCES

Achtemeier, G. L., 1986: The impact of data boundaries upon a successive corrections objective analysis of limited-area datasets. *Mon. Wea. Rev.,* **114,** 40–49.

Arnott, N. R., Y. P. Richardson, J. M. Wurman, and J. Lutz, 2003:

A solar alignment technique for determining mobile radar pointing angles. Preprints, *31st Int. Conf. on Radar Meteorology,* Seattle, WA, Amer. Meteor. Soc., 492–494.

——, ——, ——, and E. N. Rasmussen, 2006: Relationship between a weakening cold front, misocyclones, and cloud development on 10 June 2002 during IHOP. *Mon. Wea. Rev.,* **134,** 311–335.

Barnes, S. L., 1973: Mesoscale objective map analysis using weighted time-series observations. NOAA Tech. Memo. ERL NSSL-69, 60 pp. [NTIS COM-73-10781.]

——, 1994: Applications of the Barnes objective analysis scheme. Part I: Effects of undersampling, wave position, and station randomness. *J. Atmos. Oceanic Technol.,* **11,** 1433–1448.

Benjamin, S., and N. Seaman, 1985: A simple scheme for objective analysis in curved flow. *Mon. Wea. Rev.,* **113,** 1184–1198.

Betts, A. K., 1984: Boundary layer thermodynamics of a High Plains severe storm. *Mon. Wea. Rev.,* **112,** 2199–2211.

Biggerstaff, M. I., and Coauthors, 2005: The Shared Mobile Atmospheric Research and Teaching radar: A collaboration to enhance research and teaching. *Bull. Amer. Meteor. Soc.,* **86,** 1263–1274.

Buban, M. S., 2005: The dryline on 22 May 2002 during IHOP: Ground-radar and in-situ data analyses of the dryline and boundary layer evolution. M.S. thesis, School of Meteorology, University of Oklahoma, 71 pp.

——, C. L. Ziegler, E. N. Rasmussen, and Y. P. Richardson, 2005: The structure and evolution of the dryline and surrounding boundary layer on 22 May 2002 during IHOP. Preprints, *11th Conf. on Mesoscale Processes,* Albuquerque, NM, Amer. Meteor. Soc., CD-ROM, J6J.3.

——, ——, ——, and ——, 2007: The dryline on 22 May 2002 during IHOP: Ground-radar and in situ data analyses of the dryline and boundary layer evolution. *Mon. Wea. Rev.,* **135,** 2473–2505.

Demoz, B., and Coauthors, 2006: The dryline on 22 May 2002 during IHOP_2002: Convective-scale measurements at the profiling site. *Mon. Wea. Rev.,* **134,** 294–310.

Dosio, A., J. V.-G. de Arellano, A. A. M. Holtslag, and P. J. H. Builtjes, 2005: Relating Eulerian and Lagrangian statistics for the turbulent dispersion in the atmospheric convective boundary layer. *J. Atmos. Sci.,* **62,** 1175–1191.

Fabry, F., 2006: The spatial variability of moisture in the boundary layer and its effect on convection initiation: Project-long characterization. *Mon. Wea. Rev.,* **134,** 79–91.

Fedorovich, E., R. Conzemius, and D. Mironov, 2004: Convective entrainment into a shear-free, linearly stratified atmosphere: Bulk models reevaluated through large eddy simulations. *J. Atmos. Sci.,* **61,** 281–295.

Geerts, B., R. Damiani, and S. Haimov, 2006: Finescale vertical structure of a cold front as revealed by an airborne Doppler radar. *Mon. Wea. Rev.,* **134,** 251–272.

Koch, S. E., M. desJardins, and P. J. Kocin, 1983: An interactive Barnes objective map analysis scheme for use with satellite and conventional data. *J. Climate Appl. Meteor.,* **22,** 1487–1503.

Kuznetsov, L., K. Ide, and C. Jones, 2003: A method for assimilation of Lagrangian data. *Mon. Wea. Rev.,* **131,** 2247–2260.

Lazzara, M. A., and Coauthors, 1999: The Man computer Interactive Data Access System: 25 years of interactive processing. *Bull. Amer. Meteor. Soc.,* **80,** 271–284.

McCalla, T. R., 1967: *Introduction to Numerical Methods and FORTRAN Programming.* Wiley, 359 pp.

Mohr, C. G., L. J. Miller, R. L. Vaughan, and H. W. Frank, 1986: The merger of mesoscale datasets into a common Cartesian format for efficient and systematic analyses. *J. Atmos. Oceanic Technol.,* **3,** 144–161.

Oye, R., C. Mueller, and S. Smith, 1995: Software for radar translation, visualization, editing, and interpolation. Preprints, *27th Conf. on Radar Meteorology,* Vail, CO, Amer. Meteor. Soc., 359–361.

Pauley, P. M., and X. Wu, 1990: The theoretical, discrete, and actual response of the Barnes objective analysis scheme for one- and two-dimensional fields. *Mon. Wea. Rev.,* **118,** 1145–1163.

Rasmussen, E. N., R. Davies-Jones, and R. L. Holle, 2003: Terrestrial photogrammetry of weather images acquired in uncontrolled circumstances. *J. Atmos. Oceanic Technol.,* **20,** 1790–1803.

Rust, W. D., D. W. Burgess, R. A. Maddox, L. C. Showell, T. C. Marshall, and D. K. Lauritsen, 1990: Testing a mobile version of a Cross-Chain Loran Atmospheric (M-CLASS) Sounding System. *Bull. Amer. Meteor. Soc.,* **71,** 173–180.

Sanders, F., 1955: An investigation of the structure and dynamics of an intense surface frontal zone. *J. Meteor.,* **12,** 542–552.

Segal, M., and R. W. Arritt, 1992: Nonclassical mesoscale circulations caused by surface sensible heat flux gradients. *Bull. Amer. Meteor. Soc.,* **73,** 1593–1604.

Straka, J. M., E. N. Rasmussen, and S. E. Fredrickson, 1996: A mobile mesonet for fine scale meteorological observations. *J. Atmos. Oceanic Technol.,* **13,** 921–936.

Stull, R. B., 1985: A fair-weather cumulus cloud classification scheme for mixed-layer studies. *J. Climate Appl. Meteor.,* **24,** 49–56.

Trapp, R. J., and C. A. Doswell III, 2000: Radar data objective analysis. *J. Atmos. Oceanic Technol.,* **17,** 105–120.

Wakimoto, R. M., H. V. Murphey, E. V. Browell, and S. Ismail, 2006: The "triple point" on 24 May 2002 during IHOP. Part I: Airborne Doppler and LASE analyses of the frontal boundaries and convection initiation. *Mon. Wea. Rev.,* **134,** 231–250.

Weckwerth, T. M., and D. B. Parsons, 2006: A review of convection initiation and motivation for IHOP_2002. *Mon. Wea. Rev.,* **134,** 5–22.

——, J. W. Wilson, and R. M. Wakimoto, 1996: Thermodynamic variability within the convective boundary layer due to horizontal convective rolls. *Mon. Wea. Rev.,* **124,** 769–784.

——, and Coauthors, 2004: An overview of the International H_2O Project (IHOP_2002) and some preliminary highlights. *Bull. Amer. Meteor. Soc.,* **85,** 253–277.

Weiss, C. C., H. B. Bluestein, and A. L. Pazmany, 2006: Finescale radar observations of the 22 May 2002 dryline during the International H_2O Project (IHOP). *Mon. Wea. Rev.,* **134,** 273–293.

Wurman, J., 2001: The DOW mobile multiple-Doppler network. Preprints, *30th Int. Conf. on Radar Meteorology,* Munich, Germany, Amer. Meteor. Soc., 95–97.

——, and S. Gill, 2000: Finescale radar observations of the Dimmitt, Texas (2 June 1995), tornado. *Mon. Wea. Rev.,* **128,** 2135–2164.

——, J. Straka, E. Rasmussen, M. Randall, and A. Zahrai, 1997: Design and deployment of a portable, pencil-beam, pulsed, 3-cm Doppler radar. *J. Atmos. Oceanic Technol.,* **14,** 1502–1512.

Ziegler, C. L., and C. E. Hane, 1993: An observational study of the dryline. *Mon. Wea. Rev.,* **121,** 1134–1151.

——, and E. N. Rasmussen, 1998: The initiation of moist convec-

tion at the dryline: Forecasting issues from a case study perspective. *Wea. Forecasting,* **13,** 1106–1131.
——, W. Martin, R. A. Pielke Sr., and R. L. Walko, 1995: A modeling study of the dryline. *J. Atmos. Sci.,* **52,** 263–285.
——, T. J. Lee, and R. A. Pielke Sr., 1997: Convective initiation at the dryline: A modeling study. *Mon. Wea. Rev.,* **125,** 1001–1026.
——, E. N. Rasmussen, Y. P. Richardson, R. M. Rabin, and M. S. Buban, 2003: Relation of radar-derived kinematic features and in-situ moisture to cumulus development on 24 May 2002 during IHOP. Preprints, *31st Int. Conf. on Radar Meteorology,* Seattle, WA, Amer. Meteor. Soc., CD-ROM, 11A.7.
——, D. Kennedy, and E. N. Rasmussen, 2004: A wireless network for collection and synthesis of mobile mesoscale weather observations. *J. Atmos. Oceanic Technol.,* **21,** 1659–1669.
——, E. N. Rasmussen, M. S. Buban, Y. P. Richardson, L. J. Miller, and R. M. Rabin, 2007: The "triple point" on 24 May 2002 during IHOP. Part II: Ground-radar and in situ boundary layer analysis of cumulus development and convection initiation. *Mon. Wea. Rev.,* **135,** 2443–2472.